Arctic Multilayer Clouds Require Accurate Thermodynamic Profiles and Efficient Primary and Secondary Ice Processes for a Realistic Structure and Composition

Gabriella Wallentin[1], Annika Oertel[1], Luisa Ickes[2], Peggy Achtert[3], Matthias Tesche[3], and Corinna Hoose[1]

[1]Institute for Meteorology and Climate Research Troposphere Research (IMKTRO), Karlsruhe Institute of Technology (KIT), Karlsruhe, Germany
[2]Department of Space, Earth and Environment, Chalmers University, Gothenburg, Sweden
[3]Leipzig Institute for Meteorology, Leipzig University, Leipzig, Germany

Correspondence: Gabriella Wallentin (gabriella.wallentin@kit.edu)

Abstract.

Multilayered clouds are frequent in the Arctic but their detailed analysis is underrepresented. Here, we simulate two cases observed during the 2019/2020 MOSAiC expedition using the ICosahedral Non-hydrostatic (ICON) model to explore the most accurate representation of these multilayer clouds. With a limited area setup, we investigate how cloud layers respond

5   to perturbations in cloud droplet activation, primary ice, and secondary ice production (SIP). Using the measured aerosol concentration, we constrain our model through a new immersion freezing parameterisation. We find that multilayered clouds are challenging to simulate in remote areas without locally assimilated thermodynamics and that large-scale biases in the global forcing carry over to high-resolution simulations. Regarding cloud microphysics, warm-temperature ice nucleating particles (INP) are crucial to model mixed-phase clouds. However, constraining the model to the observed INPs is insufficient; a factor

10   of 10^6 is required to reach observed ice mass concentrations, which is also achieved by including SIP. Breakup upon ice-ice collisions is explosive and can increase the integrated cloud ice number concentration by a factor of 10^5. Furthermore, the seeder-feeder mechanism significantly boosts snowfall by a factor of 10^3. An accurate representation of these microphysical processes is crucial to simulate multilayer clouds.

1   Introduction

15   Mixed-phase clouds are ubiquitous in the Arctic climate system (Shupe et al., 2005). While a large observational foundation has been built over the last two decades (e.g. Shupe and Matrosov, 2006; Shupe, 2011; Morrison et al., 2012) their representation in climate models (Tan and Storelvmo, 2019), regional cloud-resolving models (Klein et al., 2009; Morrison et al., 2009; Fu et al., 2019; Schäfer et al., 2024), and large eddy simulation (LES) models (Ovchinnikov et al., 2014; Bulatovic et al., 2023; Kiszler et al., 2023) remains challenging.

20   Phase partitioning in Arctic single layer mixed-phase clouds is commonly observed as a liquid cloud layer precipitating ice (Solomon et al., 2018). The cloud phase is governed by temperature and the competing growth mechanisms of liquid droplets

and ice crystals. Clouds are commonly found to be purely liquid above 0°C, where growth mechanisms lead to rain formation. Super-cooled liquid water and ice can coexist in clouds within the mixed-phase temperature regime between -38°C and 0°C. Due to the lower saturation vapour pressure over ice, frozen hydrometeors such as cloud ice, snow, graupel, and hail may

25   grow by vapour deposition at the expense of evaporating liquid droplets in an environment that is sub-saturated with respect to relative humidity (RH) over water but saturated with respect to RH over ice. Commonly known as the Wegener-Bergeron-Findeisen process (WBF) (Wegener, 1911; Bergeron, 1928; Findeisen, 1938; Korolev, 2007) this process may lead to the glaciation of the cloud under suitable environmental conditions with intermediate vertical velocities.

In the mixed-phase cloud regime, the relative abundance of cloud ice and liquid droplets is highly dependent on the presence

30   of aerosols. Cloud condensation nuclei (CCN) act as catalysts for droplet formation by reducing the supersaturation required for condensation of water vapour. These CCN are hydrophilic and/or soluble aerosols. In the Arctic, species such as locally emitted sea salt and sulfate from dimethyl sulfate (DMS) (Schmale et al., 2021) as well as anthropogenic sulfates (Udisti et al., 2016) and aged black carbon (Zieger et al., 2023) from long-range transport are the main contributors to cloud droplet formation. In general, the concentration of these species in the Arctic is very low, sometimes even forcing the dissipation of

35   clouds in this aerosol-limited environment (Mauritsen et al., 2011; Bulatovic et al., 2023; Sterzinger et al., 2022).

Ice nucleating particles (INP) are aerosols that are typically insoluble and are the reason ice is observed at temperatures above the freezing temperature of pure water droplets (at approximately -38°C (Mossop, 1954; Korolev et al., 2017)). Acting as a seed for ice nucleation, water vapour may deposit onto the INP to form ice through the deposition nucleation mechanism, while INPs immersed within liquid droplets may freeze through immersion freezing (Hoose and Möhler, 2012). The INPs in the

40   Arctic region are commonly mineral dust transported from the south, and biological (heat labile) or organic aerosols (Creamean et al., 2022) emitted with sea spray (DeMott et al., 2016). Previously, the CCN and INP concentrations in the Arctic have only been known from shorter expeditions. The Multidisciplinary drifting Observatory for the Study of Arctic Climate (MOSAiC) expedition during 2019/2020 (Shupe et al., 2022) now for the first time provides one-year-long surface-based concentrations of CCN (Koontz et al., 2019; Dada et al., 2022; Bergner et al., 2023) and INP (Creamean et al., 2022).

45   Secondary ice production (SIP) includes processes whereby multiple ice fragments are generated through interactions between frozen hydrometeors or with liquid droplets. SIP has been successfully studied in laboratory experiments (Korolev and Leisner, 2020) but the atmospheric relevance remains unclear. Out of the six hypothesised mechanisms, three have been identified as possible major contributors based on modelling studies: (i) rime-splintering (also known as the Hallet-Mossop process) (Hallet and Mossop S.C, 1974), (ii) collisional breakup upon ice-ice collisions (Takahashi et al., 1995), and (iii) droplet freez-

50   ing and shattering (Mason and Maybank, 1960). Rime-splintering, parameterised after Hallet and Mossop (1974), describes the production of small ice fragments during the adhesion and subsequent freezing of super-cooled liquid droplets when colliding with frozen hydrometeors (riming). The Hallet-Mossop process is implemented in several global models (Komurcu et al., 2014) and many cloud-resolving models (e.g. Morrison et al., 2005; Seifert and Beheng, 2006). The droplet shattering mechanism describes the ejection of ice crystals from freezing rain droplets during the phase change as a result of pressure build-up (Mason

55   and Maybank, 1960; Kleinheins et al., 2021). The collisional breakup mechanism describes the fracturing of frozen hydrometeors upon collisions with other ice particles. All these mechanisms have been shown to occur in Arctic clouds (Pasquier et al.,

2022). They are often considered as the main reason for model discrepancies in ice concentrations (Sotiropoulou et al., 2020; Zhao et al., 2021; Possner et al., 2024).

Multilayer clouds (MLCs) are defined here as vertically stacked cloud layers that are separated by a sub-saturated layer
60   with respect to ice. MLCs have a global occurrence frequency of about 20%-30% (Subrahmanyam and Kumar, 2017; Wang et al., 2016; Liu et al., 2012; L'Ecuyer et al., 2019) but have been found to be more common in the Arctic region (Herman and Goody, 1976; Intrieri et al., 2002; Vassel et al., 2019; Nomokonova et al., 2019; Vüllers et al., 2021). For instance, data from the MOSAiC campaign show a 51% occurrence of liquid-bearing MLCs (Silber and Shupe, 2022). Arctic MLCs have been studied in idealised setups (e.g. Herman and Goody, 1976; Harrington et al., 1999; Luo et al., 2008; Chen et al., 2020;
65   Bulatovic et al., 2023) and in more detail through a model intercomparison case study from the Mixed-Phase Arctic Cloud Experiment (M-PACE) campaign on the northern slopes of Alaska (Morrison et al., 2009). However, this intercomparison study explored individual liquid layers within the same cloud, rather than the separated cloud layers we focus on here. Earlier studies have shown that MLCs may form through the incomplete dissipation of a stratus cloud (Herman and Goody, 1976), due to large-scale advection (Luo et al., 2008; Morrison et al., 2009), or through the moistening and cooling of the atmosphere
70   caused by ice precipitation (melting and sublimation) in regions of weak supersaturation (Harrington et al., 1999). The cloud layers within the MLC system interact through radiation, when the presence of an upper layer reduces the radiative cooling of the lower layer (Shupe et al., 2013; Christensen et al., 2013; Turner et al., 2018; Lonardi et al., 2022). They also interact through microphysical processes such as the seeder-feeder mechanism in which frozen hydrometeors sediment from an upper layer into a lower cloud layer. This can lead to efficient dissipation of the lower cloud through the WBF mechanism (Dedekind et al.,
75   2024; Proske et al., 2021). The impact can be further enhanced by SIP (Georgakaki et al., 2022). This natural seeder-feeder mechanism may thus increase precipitation (Jian et al., 2022; Dedekind et al., 2024). For MLCs in the Arctic, the frequency and atmospheric conditions of this process are still largely unknown.

This study aims to build on the existing knowledge of Arctic multilayer clouds and to further investigate these cloud systems in a detailed and realistic perspective using the ICosahedral Non-hydrostatic (ICON) model in a limited-area mode. We inves-
80   tigate the limits to accurately model the layering of the clouds in a remote region, evaluated with the observations from the MOSAiC campaign. We further use the observed aerosol concentrations to constrain the CCN and INP parameterisations to better represent the Arctic aerosols. SIP are explored and the impacts of seeding and glaciation due to the WBF mechanism are discussed. The paper is structured as follows. The observational data from the MOSAiC campaign, used for model constraint, and evaluation, is introduced in Sect. 2. The implemented constraints are then introduced in the model setup, Sect. 3, together
85   with the microphysical parameterisations. Section 4 describes the case study and the synoptic situation. The result sections include a general evaluation of the model in Sect. 5.1 and a more detailed high-resolution evaluation of the model together with the sensitivity studies performed, in Sect. 5.2 and Sect. 5.3. The results from SIP simulations are shown in Sect. 5.4. Finally, a discussion is provided in Sect. 6.

2 The MOSAiC campaign and observational data

90 The observational data, used for model comparison and aerosol constraint, is collected from the MOSAiC campaign (Shupe et al., 2022) where the ice breaker *RV Polarstern* (Knust, 2017) was moored on an ice shelf in the high Arctic during 2019/2020. For a complete list of instruments available during the campaign please refer to Shupe et al. (2022). Atmospheric variables are taken from level 3 Vaisala RS41 6-hourly radiosondes (Maturilli et al., 2022). Cloud variables are collected from the Cloudnet database (Engelmann et al., 2023) retrieved from ground-based remote sensing instruments through the approach

95 by Illingworth (2007). Liquid water content (LWC) is calculated where liquid water path (LWP) is recorded by a Microwave Radiometer (MWR) and the Cloudnet classification algorithm flags liquid water. The uncertainty in the LWC is 15- 25 % (Frisch, 1998; Griesche et al., 2024). The ice water content (IWC) is calculated from the 35 GHz radar reflectivity factor and temperature from a forecast model using the approach by Hogan et al. (2006) with an associated uncertainty of + 40 % and - 30 %. Cloud condensation nuclei (CCN) and ice nucleating particle (INP) concentrations are used to tune the model

100 representation of cloud droplet activation and heterogeneous freezing (Sect. 3.2). Aerosol data are obtained from measurements from the Swiss aerosol container (Beck et al., 2022) and from the American Atmospheric Radiation Measurements (ARM) site (Creamean et al., 2021a; Koontz et al., 2019). Surface INP concentrations during MOSAiC were measured using total aerosol filter samples, collected every 72 hours and analysed offline using the CSU Ice Spectrometer (IS; Cremean et al.(2022). The INP concentration during the case study is shown in Fig. 1 together with the parameterisation for immersion freezing in the

105 model by Hande et al. (2015). Surface-based measurements of CCN concentrations (Koontz et al., 2019) were perturbed by local ship emissions (due to the sampling close to the ship plume) and were thus filtered using a pollution mask from Beck et al. (2022). The mean surface CCN concentration (for the chosen case study, as described in Sect. 4) at 1 % supersaturation is shown in Fig. 2 (marked with ∗), together with the original and modified parameterisations (see Sect. 3.2).

3 Model setup

110 The ICosahedral Non-hydrostatic (ICON) model (Zängl et al., 2015) is the operational forecast model of the Deutscher Wetterdienst (DWD), Germany's National Meteorological Service, since 2015 and is developed jointly by DWD, KIT, Max-Planck Institute for Meteorology (MPI-M), Deutsche Klimarechenzentrum (DKRZ), and Center for Climate Systems Modeling (C2SM). It runs on an icosahedral grid structure; a triangular grid structure projected onto the globe, efficiently removing the pole singularity problem that models with spherical coordinates struggle with (Purser, 1988). ICON has been used for global as well

115 as regional simulations in the Arctic with multiple nested domains (e.g. Kretzschmar et al., 2020; Kiszler et al., 2023). Here we make use of the triangular grid to create domains encompassing 90°N. To study clouds, we set up a case study, making use of ICON Global 13 km analysis as initial and boundary conditions. Atmospheric variables as well as mass concentration of hydrometeors are introduced at the domain boundaries at intervals of three hours. The model is run in an offline nested limited area mode with nests at 6 km (ICON domain R3B8) and a cloud-resolving scale of 1.6 km (R2B10). Further nested simulations

120 were also run at 400 m (R2B12) and 100 m (R2B14) horizontal grid spacings, marked out in Fig. 3. Each nest is provided with an initial state and boundary conditions from the output of the coarser simulation.
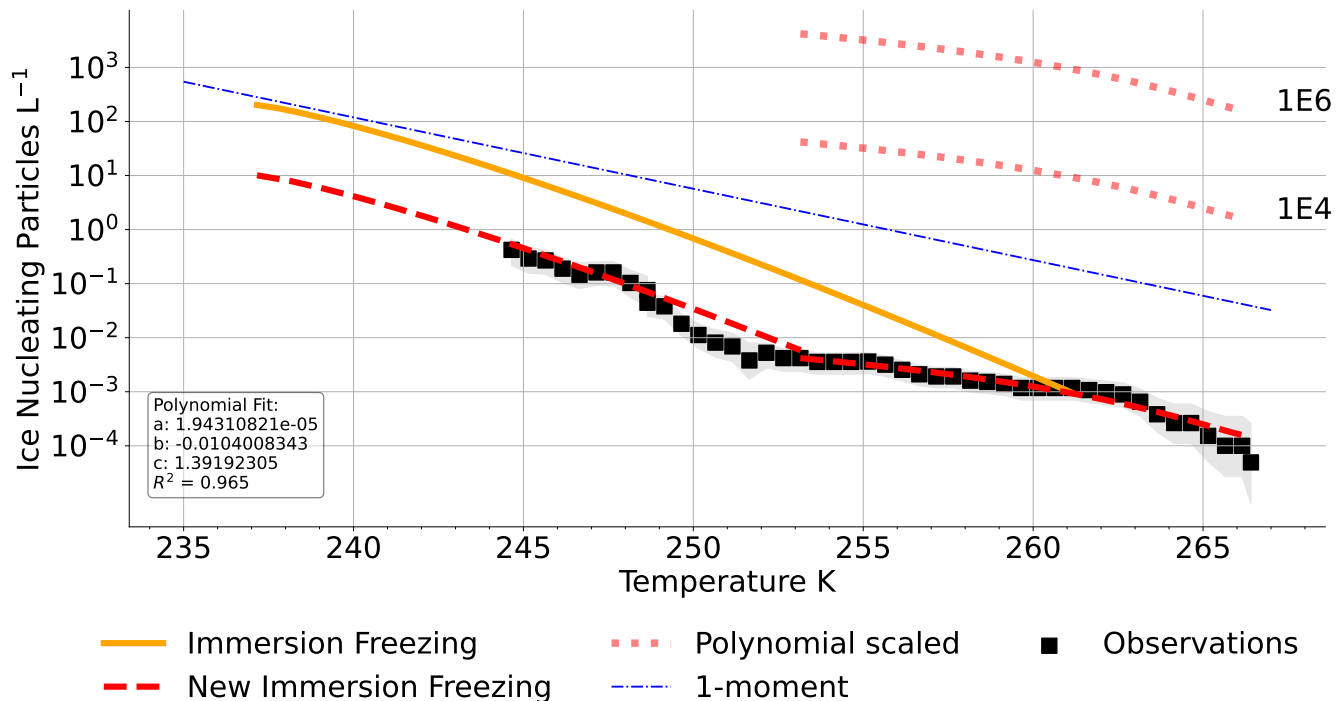
Figure 1. Ice nucleating particle concentration (L^{-1}) plotted against temperature. The immersion freezing parameterisation by Hande et al. (2015) is marked with solid orange and the observational data set (Creamean et al., 2022) in black squares with its confidence intervals indicated in shading. The observationally constrained parameterisation is shown (dashed red) where at temperatures below -20°C the original immersion parameterisation is scaled down by 0.05 while at high temperatures -20°C < T < -7°C a polynomial fit to the observational data is used with parameters indicated in the box. Perturbations to the warm INPs are shown (small dotted red) marked with 1E4 and 1E6 and the 1-moment cloud ice parameterisation by Cooper (1986) in dashed blue.

At a grid spacing of 6 km, convection is parameterised (Tiedtke, 1989; Bechtold et al., 2008) while at higher resolutions both deep and shallow convection are considered explicitly resolved. The model top is kept at 23 km while the sleeve coordinates space the model levels to keep the highest density of levels in the lowest kilometres. The 6 km and 1.6 km runs are kept to
125 90 levels while the 400 m (100 m) run is increased to 150 (200) vertical levels. At 100 m horizontal grid spacing, turbulence is partially resolved using the Lilly- Smagorinsky parameterisation (Smagorinsky, 1963; Lilly, 1962). In contrast, turbulent diffusion at coarser grid spacing is by default represented by a 2nd order closure scheme (Raschendorfer, 2001). The time step for physics (including microphysics, turbulent diffusion, and saturation adjustments) is set to 50 s, 12 s, 4 s and 0.8 s, respectively. The radiation is described by the ecRad radiation scheme (Hogan and Bozzo, 2018). We use the two-moment
130 microphysics from Seifert & Beheng (2006) with six hydrometeor classes, namely cloud droplets, rain, graupel, hail, snow, and cloud ice. The two moments refer to the first moment of the particle size distribution, the mass concentration, and the zeroth moment, the number concentration. The use of a two-moment scheme can in general improve the representation of the phase
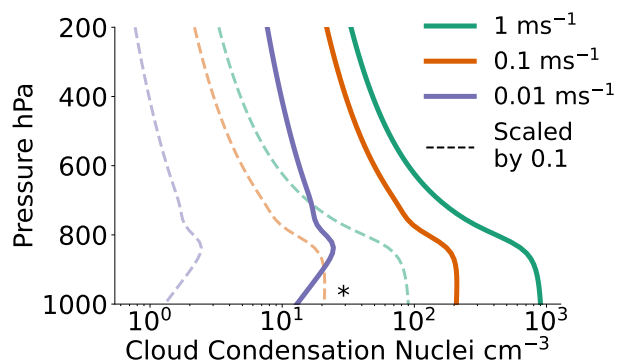
Figure 2. CCN parameterisation by Hande et al. (2016) (solid lines) giving CCN concentration (cm^{-3}) for each pressure level parameterised with respect to the vertical velocity. The observational mean value at 1 % supersaturation (Koontz et al., 2019) is marked with a * and the tuned parameterisation (divided by 10) in dashed lines.
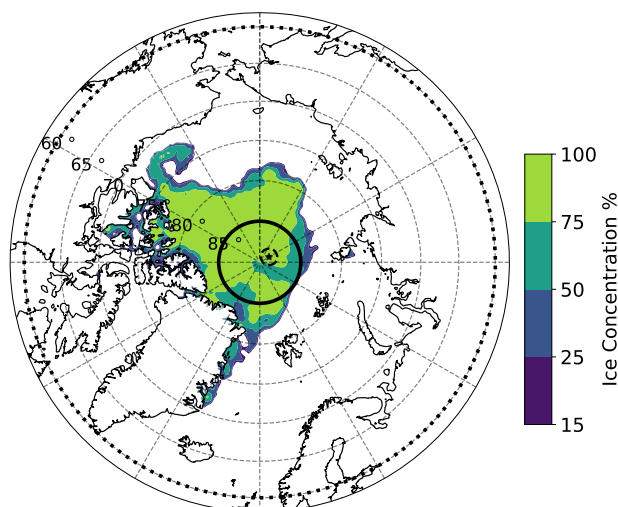
Figure 3. 1st of September sea ice concentration with the nested domains; dotted 6 km domain extending from $60°$N -$90°$N. A solid line marks the 1.6 km nest spanning $85°$N - $90°$N and a dashed marks the 400 m nest. The 100 m nest would be covered by the average daily location of the ship marked with a black star and is thus not shown. The 400 m and 100 m nests are adjusted to centre on the average daily position of the ship.

partitioning in mixed-phased clouds (Seifert and Beheng, 2006). The model is initialised at 00 UTC for the 6-km nest, and the other nests are initialised at 04 UTC, 06 UTC, and 08 UTC, respectively, to account for model spin up at a coarser resolution
135   before further increasing the horizontal and vertical resolution. This relatively short spin-up time was deemed necessary to accurately capture the local thermodynamic state. The 400 m nests (and subsequent 100 m) are initialised by the 1.6-km output, specifically the prescribed $1 L^{-1}$ simulation (see Sect. 3.2). Further increases in resolution beyond 1.6 km have only

minor impact on the cloud systems, this is shown in the Appendix A. It is hence concluded that the 1.6-km grid spacing is a good compromise between resolution and computational costs. Hourly accumulated microphysical process rates are collected with the model output and used as diagnostic indicators for which processes contribute to layer growth as well as cloud phase partitioning.

3.1 Treatment of cloud microphysical processes

3.1.1 Cloud droplet formation

The parameterisation by Hande et al. (2016), developed for ICON using its predecessor, Consortium for Small Scale Modelling (COSMO), is used for the cloud condensation nuclei (CCN) activation. This CCN activation scheme is based on the High Definition Clouds and Precipitation for advancing Climate Prediction (HD(CP)^2) Observational Prototype Experiment (HOPE) in 2013 and builds on a previous CCN parameterisation by Abdul-Razzak and Ghan (2000) and simulated aerosol concentrations. CCN activation is parameterised with respect to vertical velocity and is thus highly resolution-dependent. Perturbations to study the MLC sensitivity to CCN are explored in this paper and the modified parameterisation is shown in Fig. 2 together with the scaling towards observations.

3.1.2 Primary cloud ice formation

There are five major pathways of primary ice production in ICON, three heterogeneous and two homogeneous nucleation modes. We distinguish between freezing (ice formation from the liquid phase) and deposition nucleation (instant ice formation from vapour deposition). The three heterogeneous ice nucleation pathways are deposition nucleation, immersion freezing of cloud droplets, and the freezing of rain droplets. Deposition nucleation is the instant freezing of vapour deposited onto an aerosol while immersion freezing is the freezing of a cloud droplet containing an insoluble INP. Deposition nucleation and immersion freezing are parameterised based on simulated aerosols for Germany (Hande et al., 2015), both require ice supersaturation and activate at temperatures between -53°C < T < -20°C and -36°C < T < -12°C, respectively. Immersion freezing takes precedence wherever there are cloud droplets available. Rain freezing is counted as a source of primary ice as rain droplets implicitly contain many INPs. The freezing of a raindrop is described by Bigg (1953) and is based on probabilities of freezing depending on the volume of the droplet and temperature. Rain freeze is the only ice production mechanism above -12°C currently implemented. Contact freezing is not considered.

3.1.3 Secondary ice production

Secondary ice production includes microphysical processes where fragments of ice are generated from existing ice. SIP effectively increases ice number concentrations and is known to "fill the gap" between observed and modelled ice crystal number concentrations (Sotiropoulou et al., 2020; Zhao and Liu, 2022). Three SIP pathways have been implemented in the configuration of ICON used for this study: droplet freezing and shattering, rime-splintering (Hallet-Mossop process), and breakup upon ice-ice collisions (Han et al., 2024). The clouds investigated here exist in the temperature range of rime-splintering (-

8°C < T < -3°C), collisional breakup (-35°C <T < 0°C), and droplet shattering (T < 0°C). Thus, all three mechanisms are
170   evaluated. Rime-splintering is already included in the reference setup for ICON. This process has been found to be weak when
acting alone but in combination with ice multiplication from breakup upon ice-ice collisions, it has been shown to have a con-
siderable impact on Arctic clouds (Sotiropoulou et al., 2020; Schäfer et al., 2024). Rime-splintering is parameterised based on
the observations of Hallet and Mossop (1974). The droplet shattering mechanism, describing the process where freezing rain
droplets may fragment into smaller ice particles, is parameterised by Sullivan et al. (2018). The collisional breakup mechanism
175   requires collisions in the cloud whereby impacts between ice and snow, graupel or hail, plus all the combinations of these
(except ice-ice collisions), produce ice fragments. The breakup collision mechanism is investigated using the parameterisation
developed for COSMO by Sullivan et al. (2018) based on the laboratory work of Takahashi et al. (1995). This parameterisation
has been questioned for its atmospheric efficiency (Sotiropoulou et al., 2021; Dedekind et al., 2021; Georgakaki et al., 2022;
Han et al., 2024) due to the original experiment being conducted with large (1.8 cm diameter) colliding particles. To this effect
180   we further investigate a breakup collision parameterisation based on Takahashi et al. (1995) with a diameter scaling used in
multiple studies (e.g., Sotiropoulou et al., 2021; Georgakaki et al., 2022; Han et al., 2024). For detailed implementation in
ICON please refer to Han et al. (2024).

3.2   Constraining the microphysical parameterisations

The phase partitioning of a cloud is highly dependent on the microphysical parameterisations. We hypothesise that the INPs
185   must be adequately represented so as not to overestimate the impact of heterogeneous ice nucleation on ice clouds at low
temperatures. Similarly, the INP species active at higher temperatures need to be included to achieve a mixed-phase state
at warmer, but sub-zero, temperatures. In the 6 km run, using a 1-moment microphysics scheme, the ice crystal number
concentration is simply parameterised by an exponential function depending on temperature (Fig. 1) (Cooper, 1986). The
output from this nest is used to run the high-resolution simulation where we can make use of the 2-moment scheme in ICON.
190   In this setup both mass and number concentrations are traced in time and we can use more sophisticated parameterisations of
primary ice production to better represent mixed-phase clouds (Seifert and Beheng, 2006).

Due to the lack of an INP parameterisation developed for the Arctic, we use the ground-based observations from the MO-
SAiC campaign (see Sect. 2) to constrain the primary ice production. A factor of 0.05 is applied at cold temperatures (T < -
20°C) to the parameterisations for rain freeze, deposition nucleation and immersion freezing, following the comparison to the
195   observational values of INPs (see Fig. 1). These three parameterisations are all adjusted by the same factor as they produce ice
crystals through heterogeneous ice nucleation processes. To better represent warm mixed-phase clouds we adjust the immersion
parameterisation and add INPs at high temperatures (-20°C < T < -7°C), fitting a second-order polynomial to the observational
INP data. Rain freeze is, however, kept scaled down for all temperatures to limit the impact of the increased rain production
for scaled CCN concentrations. INPs activating as immersion nuclei at temperatures above (below) -20°C will from now on be
200   called warm (cold) INPs.

To investigate whether these constraints are appropriate, sensitivity studies have been performed and are tabulated in Table 1.
These are applied to the nest with a grid spacing of 1.6 km, initialised and updated through the boundaries with the output from

Table 1. Sensitivity simulations on the 1st and 3rd of September 2020 at 1.6 km grid spacing. BR and DS signify the SIP breakup upon collision and droplet shattering respectively while rime splintering is included in the all runs. "Warm" refers to the temperature range -20°C < T < -7°C. For more details please refer to the text.

Name	INP	CCN	SIP	Day
1.6km	original			1st & 3rd
INP	constrained			1st & 3rd
$pr_{1L^{-1}}$	1 L^{-1} at warm T			1st & 3rd
$pr_{1L^{-1}}$ + CCN	1 L^{-1} at warm T	0.1		3rd
INPx1E4	constrained + warm**x**1E4			3rd
INPx1E6	constrained + warm**x**1E6			3rd
SIP	constrained		BR & DS	3rd
SIP scaled	constrained		BR scaled & DS	3rd
$pr_{1L^{-1}}$ + SIP	1 L^{-1} at warm T		BR & DS	3rd

the 6 km simulation. To obtain the observed state and explore the sensitivity of the clouds to changes in aerosols, perturbations to the parameterisations are performed.

205   Sensitivity tests on the primary ice production include the constrained parameterisation introduced above named "INP" in Table 1 and further perturbations to the polynomial fit at warm temperatures, these are indicated by "warm". A prescribed INP concentration of 1 L^{-1} ($pr_{1L^{-1}}$ simulation) has also been applied for a uniform concentration at "warm temperatures" of -20°C < T < -7°C, while at cold temperatures the heterogeneous processes are scaled down (by 10^{-3}, effectively to zero), this setup is further perturbed with a CCN scaling to explore the sensitivity to cloud droplet activation.

210   Secondary ice processes are also explored through various SIP simulations. The three SIP simulations tabulated include droplet shattering and collisional breakup (with all runs including rime-splintering). For the breakup upon collision mechanism, we apply the parameterisation by Takahashi et al. (1995) and further explore the diameter scaling introduced in Sect. 5.4. These two SIP setups are run using the new INP parameterisation for primary ice production. To investigate the primary ice impact on SIP we further use a prescribed INP concentration of 1 L^{-1} (at -20°C < T < -7°C) and apply the Takahashi et al. (1995)
215 breakup parameterisation.

4   Case description

The 1st to the 3rd of September 2020 (from now on called the 1st, 2nd, and 3rd), during the MOSAiC campaign, were chosen to investigate two different multilayer cloud systems. On the 1st, a high ice cloud overlaying a mixed-phase boundary layer cloud can be seen in Fig. 4a showing the derived LWC and IWC products from Cloudnet (Engelmann et al., 2023). The 2nd comes
220 with a shallow lower layer and a shorter mixed-phase cloud overlapping. On the 3rd, a double-layered system can be seen in the lowest kilometre of the atmosphere with some sporadic third layers (around 2-4 km). Crosses (circles), in Fig. 4a, mark
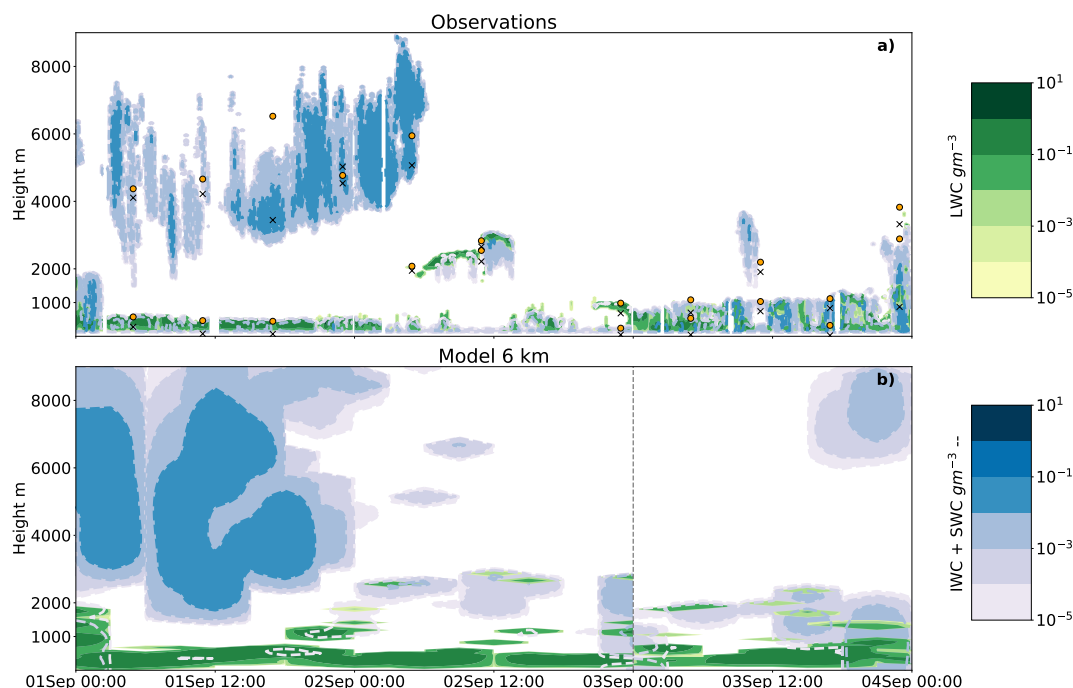
Figure 4. 3-day case study in September 2020, with the liquid water mass content (green) and cloud ice water mass content (filled contours in blue and dashed outlines). (a) 10 min observational mean, (b) 3-hourly model output at 6 km grid spacing, here also the snow water content from the model is included. The vertical line partitions the two simulations performed. Crosses (circles) in (a) mark the cloud base (top) for each layer identified using the MLC algorithm by Vassel et al. (2019).

the cloud base (top) for each layer identified using the MLC algorithm by Vassel et al. (2019). This algorithm uses radiosonde data and radar input to determine if a profile contains multiple layers and can distinguish cloud layers remarkably well. We define MLCs as cloud layers with an interstitial layer subsaturated with respect to ice with a separation of at least 100 m, following Tjernström and Graversen's (2009) determination of the lower tropospheric thermal structure. No phase distinction is applied in the classification (all overlapping clouds are accounted for independent of phase). For detailed descriptions of the observational algorithm please refer to the original paper by Vassel et al. (2019) and an updated algorithm in Achtert et al. (2024).

4.1 Synoptic situation

The synoptic situation from the model output at 00UTC on the 1st can be seen in Fig. 5. Temperatures are usual for the time of the year with the sea ice temperature locked to 273 K due to the melting of the sea ice and mean sea level pressure is shown in contours. To understand air mass origin, 10-h backward trajectories are calculated with LAGRANTO (Wernli and Davies, 1997; Sprenger and Wernli, 2015) based on hourly 3D wind fields from the 6 km simulation. Trajectories are initialised hourly between 10 UTC and 12 UTC near the ship location every 6 km within 114°E-120°E and 88.3°N-88.5°N on the 1st and within
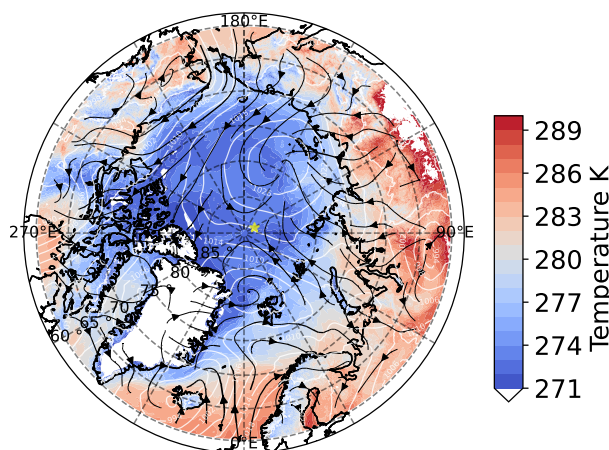
Figure 5. Synoptic situation on the 1st September. Mean sea level pressure contours are marked in white with wind streamlines (black arrows) showing the relative magnitude and direction of the wind at 10 m. The filled contours are the surface temperature. The average daily location of the ship is shown with a star (*) (1st; 88.3°N, 117°E, 3rd; 88.7°N, 120°E).

118°E-120°E and 88.5°N-89°N on the 3rd. Vertical trajectory starting positions are set to every 250 m in the lowest 2 km, every 500 m between 2 to 7 km height, and finally every 1 km up to 10 km height. Back trajectories initialised at 12 UTC on the 1st (Fig. B1) show upper-level air parcels moving faster towards the ship compared to the < 4 km trajectories, which spend more time over the pack-ice. Interestingly, on the 3rd air parcel trajectories below 2 km height move faster and originate from further away than trajectories at higher altitudes, which is likely related to the presence of low-level jets (López-García et al., 2022). Low-level winds, with magnitudes in the lowest km of up to 15 ms^{-1}, primarily flow towards the ship location from the Siberian coast, shifting from approximately parallel to the 70°E meridian on the 1st to 100°E meridian on the 3rd.

5 Results

5.1 Modelling MLCs

A first reference run is performed at 6 km grid spacing to evaluate the model against observations. Although a side-by-side comparison is difficult due to differences in spatial and temporal output, general features can be assessed. Figure 4 shows a time-height cross-section from an Eulerian perspective. The hydrometeor content derived from the observations (Fig. 4a) is compared to the model output (Fig. 4b). The model runs from 00 UTC on the 1st of Sept until 00 UTC on the 3rd. Another simulation is then initialised at 00UTC on the 3rd to prevent the model from deviating too far from the global analysis. The first 6 hours are considered spin-up and are not included in mean state analyses but are shown here for initialisation comparison. The mean state is calculated for grid points within a radius of 15 km of the ship to account for the daily drift of the ship and spatial variability. Overall, the location and timing of cloud formation in the simulation agrees well with the observations. The
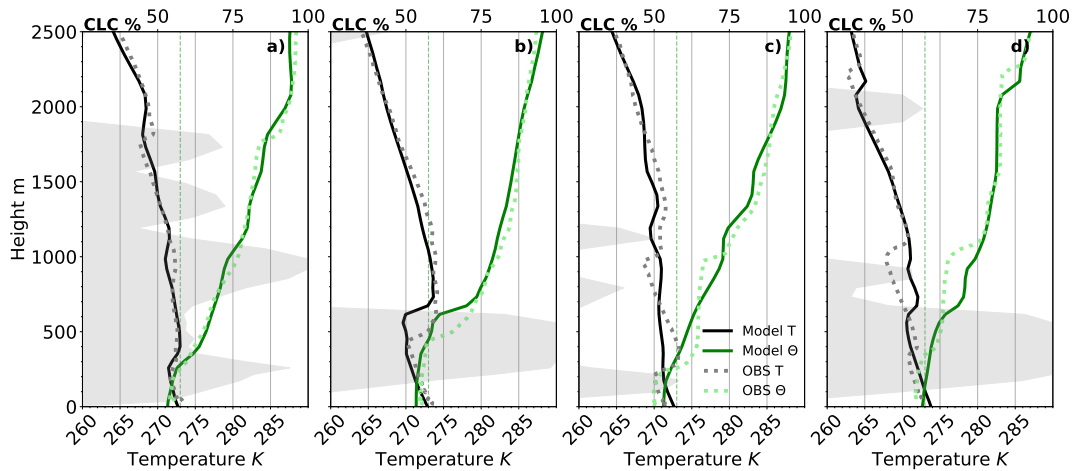
Figure 6. Vertical profiles of the lowest layer(s) for temperature (black), potential temperature (θ) (green), and the modelled cloud cover (CLC) (contours in temperature plot) signifying the cloud layers. (a) 1st at initialisation time 00UTC, (b) 1st at 12UTC, (c) 3rd at initialisation time 00UTC, and (d) 3rd at 12UTC. The observational data (in dots) are from the radiosondes (Maturilli et al., 2022) and the model data (solid lines) are the 6 km grid spacing simulation, averaged over two grid cells within the 15 km radius of the daily average ship position. The dotted vertical line marks 273 K.

boundary layer cloud on the 1st is well represented, although the phase is predominantly liquid, unlike the observed mixed-phase character. The large vertical extent of the upper cloud on the 1st may be the result of sparse vertical levels at altitudes above 7 km together with a lack of precipitation formation (no sinks). Moisture profiles compare well with the observations
255 (Fig. B2a-b). During the 2nd the cloud layers are less persistent in the model compared to the observations but the layers are captured at adequate heights. Due to the brief overlap of the cloud layers, this day will not be further studied in this paper. On the 3rd, two layers of clouds are simulated, one at around 500 m and the second at approximately 2 km. The lower layer cloud is well constrained to the boundary layer but liquid dominated while the upper cloud is placed 1 km higher than the observations. In general, the 6 km simulation accurately represents the clouds but falls short in representing the phase partitioning. Constraints
260 have been implemented in the microphysical parameterisations to address this issue (see next section).

The placement of these layers depends on the initialisation of the model. On the 1st (Fig 6a), the model quite accurately captures three low temperature inversions (at 300 m, 1000 m, and 1800 m) and correctly predicts the loss of the upper two in favour of a persistent layer at 600 m in the 12UTC radiosonde profile (Fig. 6b). The 3rd suffers from the lack of local data assimilation in the ICON Global analysis, deviating quite radically from the observed radiosonde profile in Fig. 6c. The strength
265 of the upper inversion at 1 km at 00UTC is not enough to sustain the cloud layer at this height and instead, an upper inversion is formed at 2 km, 1 km above the observations (Fig 6d). Excessive vertical mixing in the model is thought to cause this issue. Moisture content and relative humidity with respect to liquid water are shown in Fig. B2 for completeness. Subsequent high-resolution runs (see Appendix A) do not improve on the main layering (some spurious intermittent layers may occur with higher vertical resolution), as this is mostly governed by the initial state.
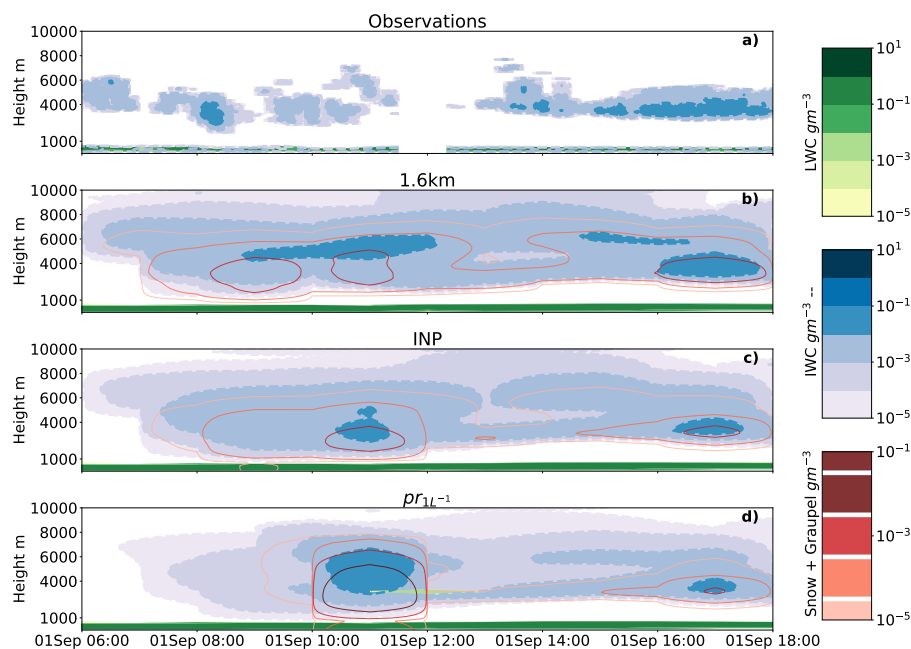
Figure 7. Vertical cross-section on 1st September 2020, with the liquid water mass content (green) and cloud ice water mass content (filled contours in blue and dashed outlines) in (a) 10 min observational mean together with (b) reference simulation, hourly model output at 1.6 km grid spacing, (c) the constrained INP simulation, and d) the prescribed $1 L^{-1}$ INP at warm temperatures. Additional model parameters shown are the graupel and snow mass content in red (solid lines).

5.2 1.6 km simulations for 1st of September

The 1st of September 2020 is further simulated with a higher resolution nest at 1.6 km, where the boundary conditions (and initialisation) are provided with input from the 6 km simulation. We make use of the 2-moment microphysics and aerosol constraints laid out in Sect. 3.2. The high-resolution simulation, similarly to the 6 km run, produces a thick ice cloud and a fully liquid lower layer, found at a temperature just below 0°C. A vertical cross-section of hydrometeors with time is shown in Fig. 7 for the original setup at 1.6 km (Fig. 7b) and the simulation with constrained INP (Fig. 7c). Compared to the observations (Fig. 7a), the model in its original setup produces too much ice in the upper layer while the lower layer is dominantly liquid compared to the observational mixed-phase character (mostly visible in Fig. 4).

With the INP constraint at cold temperatures, reduction of rain freeze and the warm INPs acting at high temperatures, surprisingly, no large impacts can be seen (Fig. 7c). Prescribing INPs at $1 L^{-1}$, (Fig. 7d), effectively increasing the immersion freezing at the bottom of the upper layer while reducing INPs at colder temperatures, renders similar cloud features with the largest difference being the intermittent liquid layer during the 10-12UTC window. This liquid layer is short-lived and dissipates by preferential vapour deposition (WBF process) onto ice and snow. We hypothesise that the liquid layer forms due to the activation of numerous INPs at this altitude (T > -20°C) causing a higher rate of collisions rendering larger falling
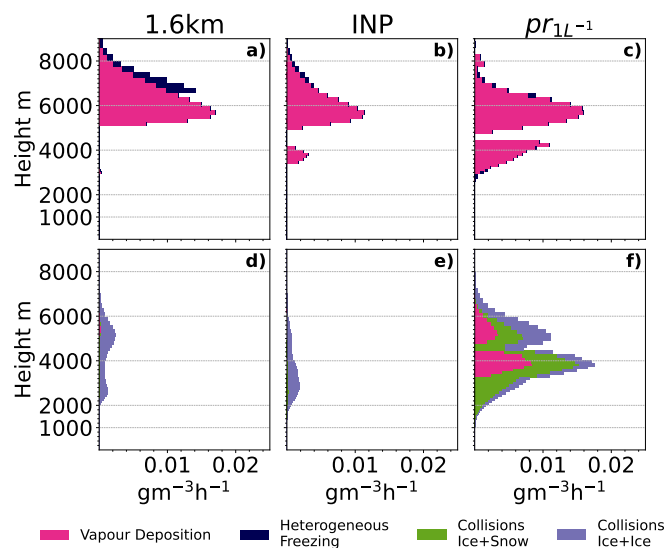
Figure 8. Microphysical process rates hourly accumulated during the simulation and here taken as a mean between 10-12UTC on the 1st of September. a-c) show processes for cloud ice, and d-f) for snow. Colours correspond to the various process rates defined in the legend. Collisions lead to aggregation where ice+ice and ice+snow give snow aggregates.

particles (process rates are shown in Fig. 8f). The liquid layer then forms due to the increase in supersaturation with respect to
285 liquid water enabled by the sublimation of the falling hydrometeors coinciding with a weak updraft. The increase in updraft
may on the other hand be due to latent heating from the increased vapour deposition in this layer (Fig. 8c). Ice-ice collisions
result in particles assigned to the snow category, while ice-snow collisions aggregate into larger snow particles (Fig. 8d-f). The
snow produced in the lower part of the upper cloud seed the lower cloud but not efficiently enough to glaciate or strengthen
it. The snow particles seemingly fall through the lower layer with negligible interactions. Both of the modelled cloud layers
290 seem quite impervious to perturbations. We accredit this negligible impact of the perturbations to the horizontal extent of the
cloud layers. From the back trajectories (Fig. B1), a pseudo-lagrangian framework is adopted. Instead of tracking the cloud
from the trajectories, we take a longitudinal mean over the area the trajectories span. Figure B3 shows the mean state of the
clouds originating from the direction of the trajectories at 10UTC and 12UTC. The lower layer extends throughout the 1.6 km
domain and an upstream analysis shows the clouds being advected from the boundary region up to the ship location in about
295 eight hours. The system is highly governed by the initial state of the model and the advection towards the ship.

5.3   1.6 km simulations for 3rd of September

The 3rd of September 2020 is also simulated at a higher grid spacing of 1.6 km using the 2-moment microphysics. The time-height contours of the 3rd are shown in Fig. 9, where the reference at 1.6 km (Fig. 9b) and the constrained INP simulation (Fig. 9c) are shown together with the observations.
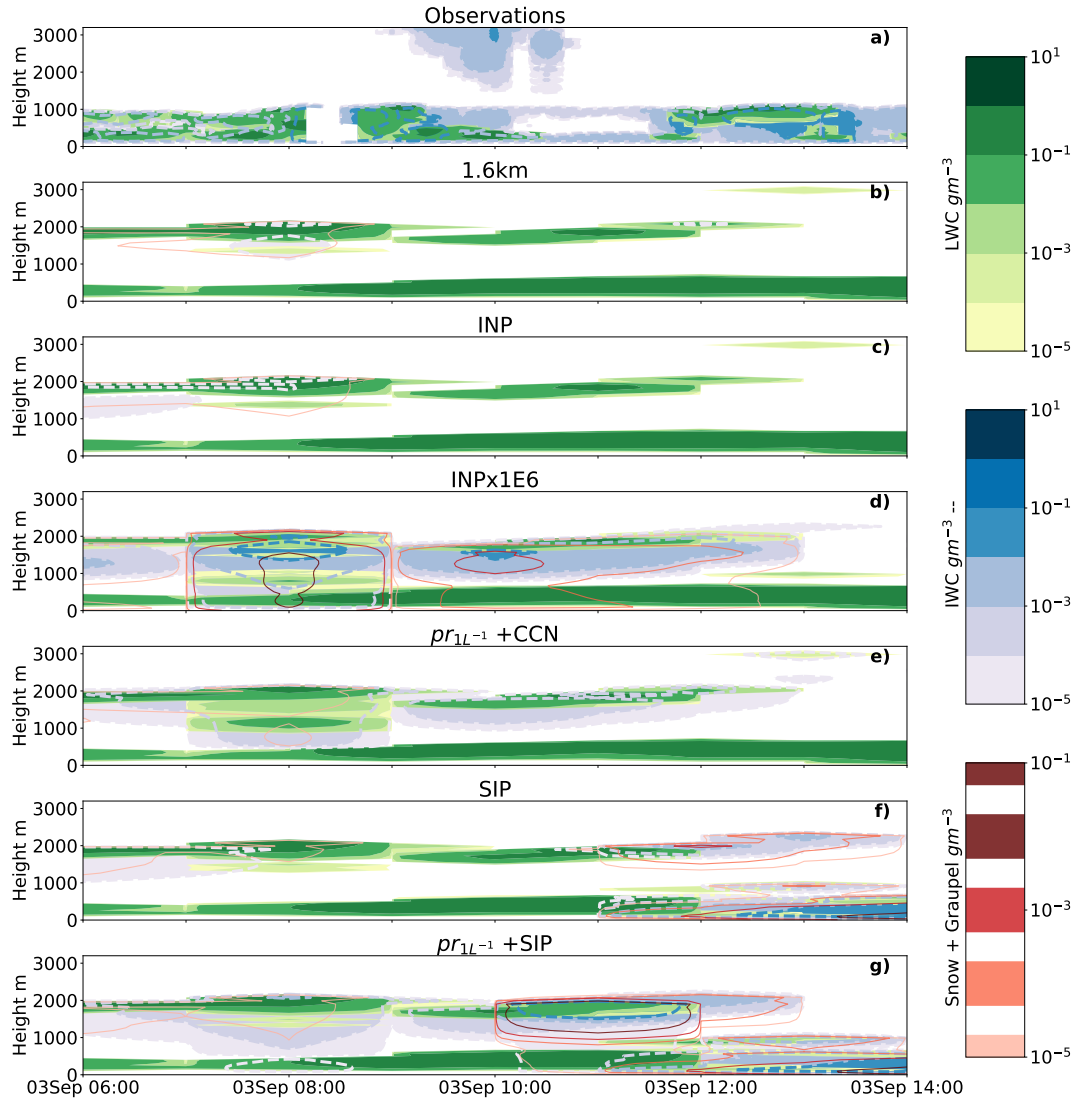
Figure 9. Time height plot of hydrometeors from the 3rd of September with liquid water mass content (green) and cloud ice water mass content (filled contours in blue and dashed outlines). (a) Observations 10 min mean, (b) reference run, (c) INP constrained simulation, (d) warm INP perturbation by 10^6, e) a prescribed INP concentration of $1L^{-1}$ at warm temperatures combined with a CCN scaling of 0.1, f) SIP using the same primary ice nucleation as the INP simulation with added droplet freezing and shattering and breakup upon ice-ice collisions, g) prescribed INP at $1L^{-1}$ with added droplet freezing and shattering and breakup upon ice-ice collisions. Additional model parameters are the snow and graupel mass content in red (solid line). For clarification on the perturbations please refer to the text and Fig. 1.

300   As previously discussed, the model layers the clouds at the wrong heights, but more striking is the lack of ice in the model. At a mean cloud-top temperature of -8°C (Fig. 6), the only primary ice parameterisation active in the reference is rain freeze, however, the addition of warm INPs (Fig. 4c) does little to increase the ice concentration. Blue contours marking the cloud ice

mass concentration can be seen to only slightly increase (mostly just after 6UTC) when including warm INPs. This small impact does not reach the observed levels of ice. Thus we explore the perturbations to the primary ice parameterisations in the model.

305 Multiplying the warm INP polynomial (Fig. 1) by 10^4 (Fig. A1b) and 10^6 (Fig. 9d), give rise to more similar values to the observations. These are very extreme perturbations, but as the observed INP concentration is low, this gives INP concentrations between 1-100 L^{-1}, on the upper end in midlatitudes and very high for Arctic clouds (Porter et al., 2022; Raif et al., 2024). With this high INP concentration, we would expect the WBF process to be efficient and glaciate the cloud. Interestingly, the mixed-phase character persists through two orders of magnitude increase in ice, potentially showing an inefficiency in the

310 WBF process as seen by other ICON studies (Omanovic et al., 2024). As a perturbation of 10^4 to 10^6 is needed to create appreciable ice content in the clouds we further explore a prescribed INP concentration at warm temperatures of 1 per L ($pr_{1L^{-1}}$), and decrease the cloud droplet activation rate ($pr_{1L^{-1}}$+ CCN), shown in Fig. A1d and Fig. 9e respectively. The prescribed INP compare well with the 10^4 perturbation, with slightly lower values for cloud ice. More interesting is perhaps the CCN perturbation where we see a third layer forming underneath the upper layer at 08UTC. This will be further discussed

315 below.

To better compare with the observed values we look at the column integrated values where we include graupel and snow together with ice in a frozen water path (FWP) category. Figure 10 shows the time-averaged (06-12UTC) FWP vs LWP.

The large underestimation (more than two orders of magnitude) of FWP in the 1.6 km simulation (circle in Fig. 10) compared to observed values (diamond) is quite evident while the LWP is approximately five times too high in the model. The small

320 change using the new INP parameterisation (INP simulation, square) gives an increase in FWP with a preference for cloud ice. The prescribed INP simulation ($pr_{1L^{-1}}$, tilted cross) looks similar in the contours to the 10^4 perturbation (right pointing triangle) but gives a three times lower FWP. This corresponds nicely to the almost three times lower INP concentrations for the prescribed INP simulation at minimum cloud-top temperatures (about -9°C).

The CCN perturbation ($pr_{1L^{-1}}$ +CCN, tilted hexagon) is an interesting simulation. As expected with a lower CCN concen-

325 tration, we see an increase in rain (colour bar of Fig. 10a). With a lower activation rate of CCN, the cloud droplets may grow to larger sizes due to less competition for vapour and convert more efficiently to rain through autoconversion. An unexpected outcome, however, is the formation of a third layer around 08UTC (Fig. 9e). We hypothesise that the sub-cloud layer (at 1 km) of the upper layer moistens through the evaporation of rain falling from the upper cloud (Fig. B4c). This initiates cooling and turbulent mixing leading to local updrafts and activation, creating a short-lived (about two hours), mixed-phase cloud un-

330 derneath the upper layer. This formation mechanism has been previously theorised by Harrington et al. (1999). Compared to our case, their cloud grew in strength with the simulation time due to the initiation of cloud-top radiative cooling. We further hypothesise that the third layer forming here is too close to the upper layer such that the radiative heating from the upper layer suppresses the long-wave cooling in this layer, causing its dissipation. To be noted, the 10^6 perturbation also obtains a third layer during the same period. This more shallow layer is instead driven by the sublimation of frozen hydrometeors in the

335 sub-saturated cloud gap (process rates are shown in Fig. B4).

Due to this increase in condensation, the impact of the CCN scaling is smaller. When reducing the CCN by a factor of 10, the LWP only drops by a factor of 1.28. We further note the twofold increase in FWP between the prescribed INP simulation
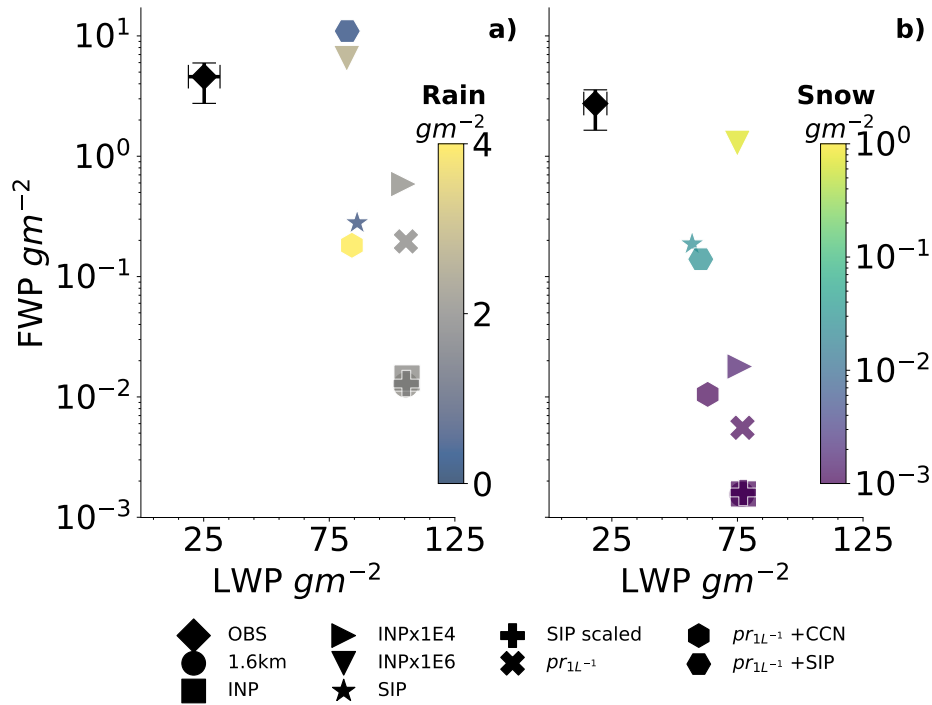
Figure 10. Frozen hydrometeor water path (FWP) the vertically integrated sum of cloud ice, snow, graupel and hail, over liquid water path (LWP) for all perturbations on the 1.6 km resolution on the 3rd of September between 06UTC-12UTC,. (a) The column integrated FWP vs LWP with colours indicating the precipitation contribution from the rain in gm^{-2}. The observations are integrated up to 1.1 km to exclude the upper ice cloud during this time. (b) FWP and LWP are integrated over the modelled lower layer with an imposed upper threshold at 750 m. The colour bar in (b) shows the snow falling from the lower layer (graupel is negligible).

and the CCN-scaled version. The presence of the sub-cloud layer with adequately large cloud droplets that may convert into rain increases the riming rate and the possibility of rime-splintering, granted the cloud exists within the temperature range of
340    $-8°C< T< -3°C$. Thus graupel forms and seeds the lower layer. The increase in the mass-accumulated riming rate of graupel can be seen in Fig. B5q and the small impact from rime-splintering in Fig. B6b. These processes are not strong enough to glaciate the lower layer, nor any classical seeder-feeder impacts can be seen.

     The large perturbations of warm INPs (INPx1E4 and INPx1E6) thoroughly increase the FWP, however highly non-linearly with a 40 (450) times increase between INP and INPx1E4 (INPx1E6). Here, we notice that the lack of glaciation in Fig. 9d
345   may not show the full story. When we look at the integrated values a 77% decrease in LWP in the upper layer between the 1.6 km and the INPx1E6 (down-pointing triangle) simulation can be seen, showing the WBF process in action together with an increase in riming by cloud droplets (Fig. B5a-b). An increase in riming may be due to the sheer number of ice particles now present in the cloud.

Looking at the lower layer only, Fig. 10b, similar trends to the full integration can be seen with a next-to-none impact of
350   simply adding the warm INPs (simulation INP). The perturbations of warm INPs (simulations INPx1E4 and INPx1E6) both
increase the FWP in the lower layer. As this layer is found at a temperature just below 0°C, this increase is due to seeding from
above. An increase in precipitation from the lower layer can also be seen with the highest INP perturbation (INPx1E6), where
snow precipitation increases by three orders of magnitude, showing the seeder-feeder mechanism in play. Interestingly, the 10^4
perturbation does not show a similar pattern of precipitation increase. Instead, this simulation shows only a large increase in
355   ice concentration. With a larger amount of activated INPs, ice crystals grow less efficiently due to the competition for water
vapour. The ice crystals largely occupy the same space and increasing the number of ice crystals in the same volume makes
collisions more likely (the collision process rates, where ice collides with ice or snow to form snow are shown in Fig. B5g-h).
Snow, with a larger size, tends to fall more readily and allows for seeding of the lower layer, explaining the larger amount of
snow (and thus FWP) for INPx1E6 in Fig. 10.

360   ## 5.4   Can the INP perturbation be explained by SIP?

Secondary ice processes may be the missing link between the observed INP concentrations and the frozen water path, which is
underestimated by the simulations discussed so far. We investigate whether the required warm INP perturbation of 10^6 detailed
above could be replaced by a (potentially) more realistic pathway. On top of the rime-splintering already implemented in the
reference, we add breakup upon ice-ice collisions as well as droplet freezing and shattering to the INP simulation setup. With
365   a mean cloud top temperature of -1.5°C (between 6-12UTC) for the lower layer on the 3rd, two out of three SIP (collisional
breakup and droplet shattering) may be active, while the upper layer at a mean cloud top temperature of -8.5°C, overlaps with
the temperature range for all three (including rime-splintering).

Three simulations have been performed and are tabulated in Table 1. Two runs explore the breakup parameterisation, using
Takahashi et al. (1995) and Takahashi scaled by the colliding particle diameters (Han et al., 2024). A third simulation explores
370   the primary ice impact on the SIP where the INP concentration at warm temperatures is set to 1 per L ($pr_{1L^{-1}}$+ SIP).

Figure 9f shows the SIP run using the parameterisation based on the unscaled data by Takahashi et al. (1995) as well as
the SIP simulation using a higher INP concentration ($pr_{1L^{-1}}$+ SIP, Fig. 9g). Overall they display similar features, with a
large increase in ice water content. This is explained by the large contribution from breakup upon collisions with the major
contributions from small ice crystals colliding with snow or snow-snow collisions (Fig. B6d). The ice-snow collisions are the
375   most active in-cloud while snow-snow collisions dominate throughout the sub-cloud layer. The rime splintering and droplet
shattering show only small contributions (Fig. B6b-c). Both SIP implementations almost fully glaciate the lower layer just after
12UTC, some liquid persists while the upper layer dissipates similarly to the other experiments (Fig. 9a-e).

The main difference between the simulations is the seeding seen with a higher baseline of INPs. This is explained by the
higher collision rates as previously discussed for a larger amount of small ice crystals (Fig. B5i,l). The mean hourly collisional
380   rate increase between the $pr_{1L^{-1}}$ + SIP and $pr_{1L^{-1}}$ (without SIP) is five orders of magnitude while the difference between
the "INP" and "SIP" simulations reaches six orders of magnitude. This increase in collisions increases the collisional breakup,

especially between ice and snow and between small ice crystals, leading to a large contribution from this scheme (Fig. B6d). This follows the findings by Sotiropolou et al. (2024) who shows the dominance of collisional breakup for Arctic clouds.

The seeding, seen in Fig. 9g, has a surprisingly small impact on the lower layer during the time window 06-12UTC, referring
385   back to Fig. 10b. The simulations with SIP implementations (cross and hexagon) do not differ in LWP nor FWP in the lower layer, showing the lack of interaction with the falling hydrometeors from the upper layer. While comparatively similar in the lower layer, in the upper layer, the $pr_{1L^{-1}}$ +SIP gives a close to two orders of magnitude higher ice content than the simulation with a lower baseline of INPs (Fig. 10a). Scaling the breakup collision parameterisation (SIP scaled), to reduce the large increase in ice crystals forming from the collisions does not change the simulation compared to the reference (Fig. 10 and
390   contours in Fig. A1c). This might be due to very small frozen hydrometeor sizes that scale down this collisional rate too much or the lack of ice habit representation.

An ice enhancement factor, the increase in the number concentration of cloud ice due to SIP, can only be used for a con-strained LES simulation where all ice within the domain has been formed during the simulation. Here, as we are dealing with a real setup, a large proportion of the ice in the domain is initialised with the model and due to the lack of sinks, survives the
395   time it takes to be advected up to the ship site. To gauge the impact of the SIP however, we may calculate the ratio between the simulations with and without SIP (apart from the rime-splintering which is included in all runs but has a small impact) by N_{SIP}/N_{Ref}, where N is the number concentration of cloud ice and "SIP" and "Ref" refer to the simulation with and without SIP (with the same initial primary ice). As can be seen in the contours in Fig. 9f-g, the SIP impact is highly time-dependent and seems to explode at 11-12UTC. The maximum ice number concentration enhancement ratio (at 11UTC for SIP simulation
400   and 12UTC for $pr_{1L^{-1}}$ + SIP) is 10^5 and 10^4 respectively (the average QNI is shown in Fig. B6e), showing a higher efficiency for a lower initial primary ice as been previously seen in the LES simulations by Sotiropoulou et al. (2020). The cloud ice mass concentration enhancement is 42 and 15 respectively while the FWP (Fig. 10) increases by a factor of 22 and 56 respectively, with the latter due to the increase in snow for the $pr_{1L^{-1}}$ + SIP run (Fig. B5).

6   Discussion and conclusions

405   In this study, we investigate the microphysical sensitivity of Arctic mixed-phase multilayer clouds via the example of two cases observed during the MOSAiC campaign. Sensitivity simulations on cloud droplet activation, primary ice, and secondary ice processes were performed for two multilayer cloud systems in September 2020. The ICON model (Zängl et al., 2015) is used to model these cloud systems and observational data from the MOSAiC campaign (Shupe et al., 2022) is used to constrain and evaluate the model. The focus of this paper is two-fold, 1) to show that multilayer clouds can be accurately modelled
410   providing a ground for further analysis into how these cloud systems form and evolve, and 2) to evaluate the microphysical sensitivities, in particular, the primary ice production and its impact on secondary ice production (SIP), while constraining the parameterisations to the observed ground-based measurements to better represent cloud phase.

Using the ICON model, a nested setup is adopted and through our analysis, we find that high resolution (grid spacing finer than 1.6 km) simulations are not necessarily needed to represent the clouds, although we acknowledge higher resolutions than

415   the 100 m studied here may be beneficial for many purposes (such as detailed studies of entrainment and turbulence, and especially idealised studies). We set up our model as a real case, with initial and boundary conditions from ICON Global 13 km analysis. The clouds are adequately represented in terms of vertical placement. However, during days when the local thermodynamic structure is not captured in the initial conditions, the model suffers from incorrectly placed cloud layers (vertical layering) as the radiosondes launched at MOSAiC were not assimilated. The local structure and layering do not improve with

420   higher resolution; these real-case setups suffer from carrying over large-scale biases in the initial and boundary conditions, which do not improve upon decreasing the grid spacing. Assimilation of available radiosondes may thus be crucial for accurate representation of these clouds.

Switching from a 1-moment microphysics scheme to a 2-moment scheme facilitates comparisons with the real world, as the primary ice is represented using more explicit freezing pathways. With the 2-moment microphysics and a 1.6 km grid spacing,

425   we perform microphysical perturbations by constraining the model parameterisations with measured data. An immersion freezing parameterisation is created based on the surface-measured INPs to better represent the Arctic INP population. Accurate representation of these clouds is challenging and to adequately represent the observed ice concentration at warmer temperatures (T > -19°C), large perturbations to the measurement-constrained immersion freezing parameterisation are needed, amounting to a factor between 10^4-10^6, which corresponds to INPs in the range of 1-100L^{-1}. We hypothesise that the addition of the

430   measured INPs is still too low to initiate further ice-phase processes, such as growth by deposition, and a larger perturbation is required to get a response.

The reduction of CCN concentration does not have a large impact on the simulations apart from an expected rain enhancement due to the formation of larger droplets. We hypothesise that the lack of CCN impact is due to the extent of the cloud layers such that the clouds are advected in through the domain boundaries. Together with continuous CCN activation, a lack of

435   strong sinks ensures the persistence of the clouds. However, we observe the formation of a third layer due to this rain formation and evaporative moistening of the sub-cloud layer, something previously theorised by Harrington et al. (1999). The cloud here, however, does not survive more than two hours. We further note similarly sporadic and shallow layers forming in perturbations with high INP concentrations where we hypothesise the formation is due to the sublimation of the frozen hydrometeors in the sub-cloud layer followed by a formation similar to above.

440   SIP have been investigated as these mechanisms are commonly thought to fill the gap in number concentration of cloud ice between models and observations. We find that the parameterisation for breakup upon ice-ice collisions (Sullivan et al., 2018) based on laboratory work by Takahashi et al. (1995) is very active, with time successfully glaciating the lower layer through the increase in small ice crystals and snow formation. The maximum enhancement in the integrated cloud ice number concentration between simulations with and without SIP amounts to 10^5-10^4, for a low and high initial INP concentration

445   respectively. These factors are on the larger side but compare well to other Arctic studies that found ice enhancement up to 10^2 (Sotiropoulou et al., 2020) and 10^4 (Zhao et al., 2021), however, the enhancement is highly fluctuating with time, making a concrete analysis into whether or not the parameterisation is correctly representing the processes challenging.

Scaling the breakup collision process by the particle diameter (Sotiropoulou et al., 2021; Georgakaki et al., 2022; Han et al., 2024) scales down the process such that no SIP impacts can be seen. Further sensitivity studies, such as scaling the pre-factor

450 in the parameterisation for breakup upon ice-ice collisions, as other studies have done (e.g. Sotiropoulou et al., 2020; Dedekind et al., 2021) may tune the collisional breakup rates to avoid the complete glaciation. Here, we will settle on the possibility that SIP may be a missing factor in these cloud layers and that we may not have the parameterisations available to properly explain the discrepancy. The dependency on initial INP concentration alludes to the misrepresentation of the INPs through our measurement-constrained parameterisation and we conclude that an INP distribution is hard to capture with a model and

455 with measurements (Burrows et al., 2022). Only ground-based measurements are available, which do not always correlate with INPs at cloud base (Creamean et al., 2021b), and we believe this may be part of the explanation. Another aspect is the lack of INP recycling in the model, whereupon INPs in the sub-cloud layer, deposited by precipitating ice, can re-enter the cloud and activate with possible time-dependent freezing rates, which is important for Arctic mixed-phase clouds (Solomon et al., 2015; Fu et al., 2019). INPs calculated from lidar measurements (Ansmann et al., 2023) may be the way forward and

460 aerosol parameterisations based on their findings together with ground-based measurements may be a useful contribution to the modelling community. Through this exploration into the most accurate ways of representing these multilayer clouds we hope to lay the foundation for further studies into how these layers form, evolve, and impact the Arctic climate system.

Data availability. ICON model output is available on request from the authors.

Appendix A: High resolution simulations

465 Clouds are sensitive to the resolution on which the simulation is done. Better representation can in general be expected when the grid spacing is decreased. When simulating these cloud layers, however, we see minimal impact on the clouds. For the 400 m run, with a finer horizontal as well as vertical grid spacing (increase from 90 to 150 vertical levels), we only see a small impact from a higher rate of droplet activation stemming from the better-resolved updrafts. The finest grid spacing simulation at 100 m changes the clouds marginally more than the 1.6 km setup and is shown for the 3rd in Fig. A1e. For the 100 m

470 simulation, the explicit turbulence parameterisation is switched on and the vertical grid spacing is increased (to 200 levels). Most impacts seem to be due to the higher vertical resolution, rendering the cloud boundaries sharper. Some collisions are initiated giving a larger contribution of snow falling into the lower layer. This is, however, not enough to have any appreciable impact on the lower layer.

On the 1st (Fig. A2b,c), the high-resolution simulations impose sharper cloud boundaries, similar to the 3rd, and the upper

475 cloud obtains more individual features due to the increased vertical resolution. The cloud liquid increases due to more resolved updrafts.
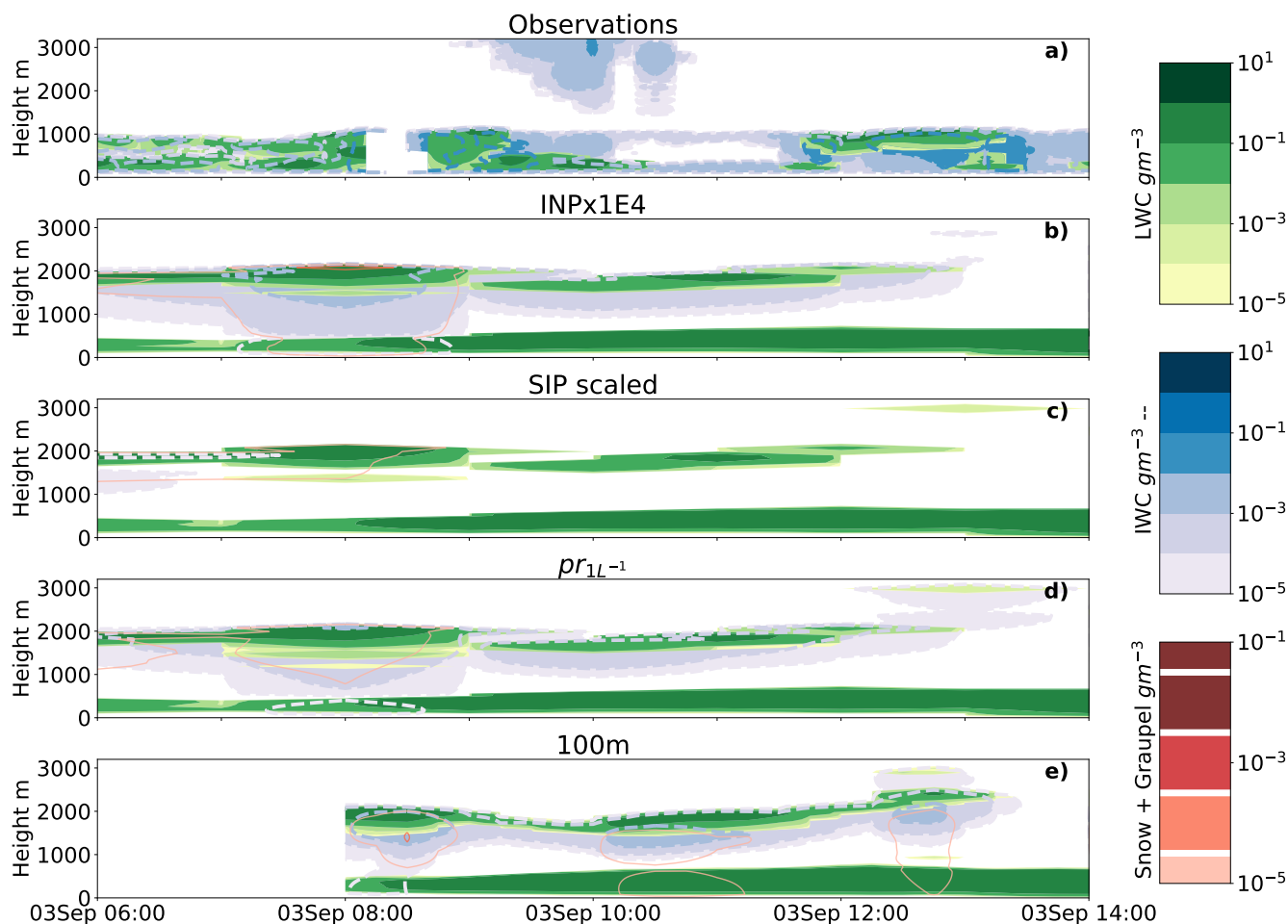
Figure A1. Time height plot of hydrometeors from the 3rd of September with liquid water mass content (green) and cloud ice water mass content (filled contours in blue and dashed outlines). (a) Observations 10 min mean, (b) polynomial perturbation of 10^4, (c) SIP simulation with a scaled breakup upon ice-ice collision parameterisation, d) the prescribed INP to 1 per L at warm temperatures and, (e) 100 m simulation initialised using $pr_{1L^{-1}}$ with a subsequent nest at 400 m grid spacing. Due to a 2 h delay between nests, the 100 m nest is only initialised at 08UTC. Additional model parameters are the snow and graupel mass contents in red (solid line).
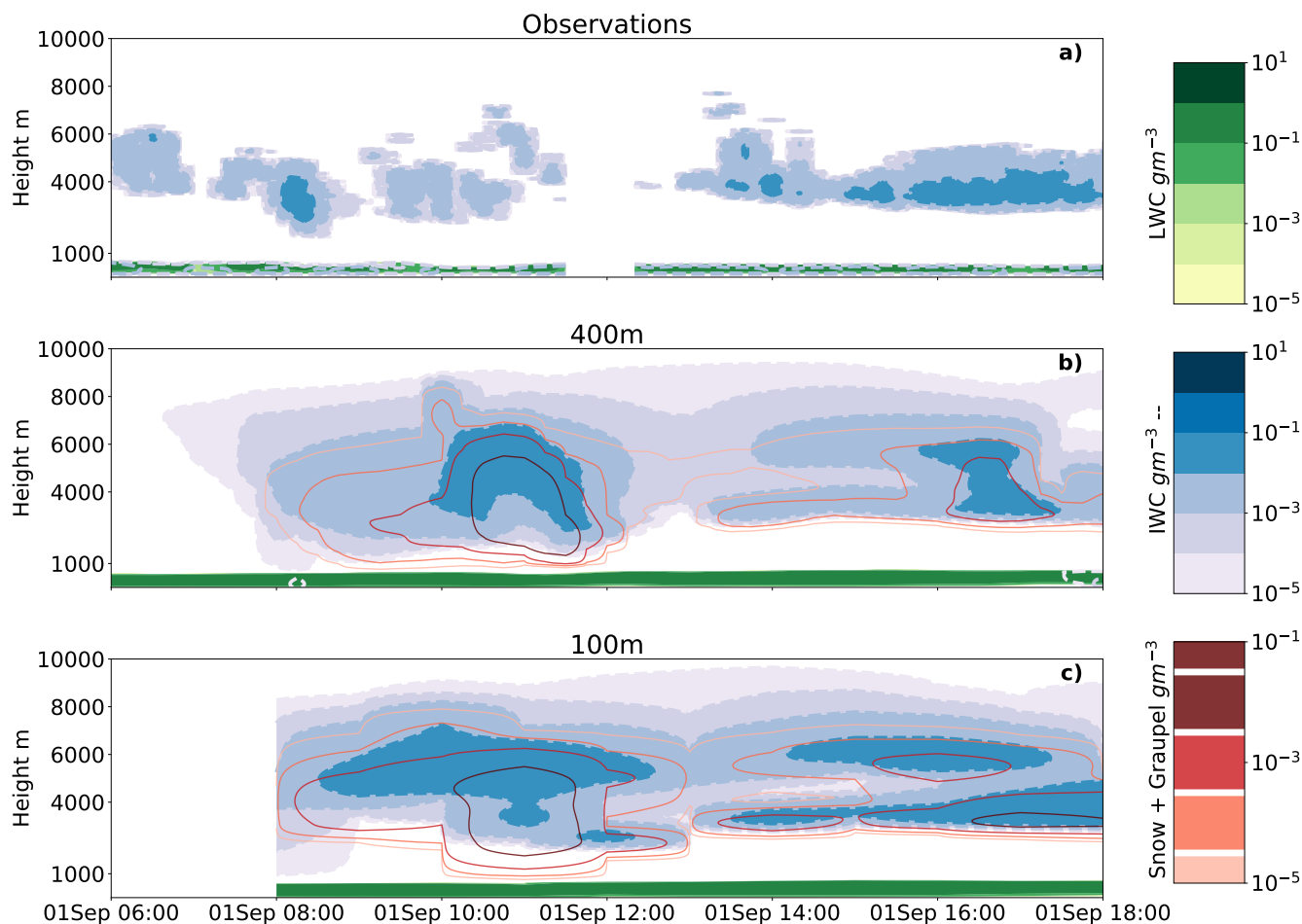
Figure A2. Time height plot of hydrometeors from the 1st of September with liquid water mass content (green) and cloud ice water mass content (filled contours in blue and dashed outlines). (a) Observations 10 min mean, (b) 400 m, initialised from the output of pr_{1L-1} and, (c) 100 m initialised using the 400 m simulation. Due to a 2 h spin-up between nests, the 400 m (100 m) nest is only initialised at 06UTC (08UTC). Additional model parameters are the snow and graupel mass contents in red (solid line).

Appendix B
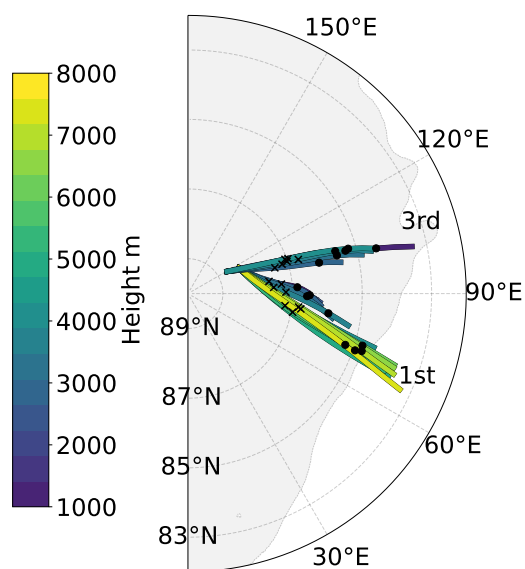
Figure B1. Back trajectories initialised at the daily average ship location at 12UTC for the 1st and 3rd of September, the dates are marked at the end of the trajectory cluster. Colours indicate the height at which the back trajectory is initialised and crosses (dots) mark 8UTC (4UTC). For the 3rd, only trajectories initialised at 4 km or lower are shown because of the low clouds during the 3rd.
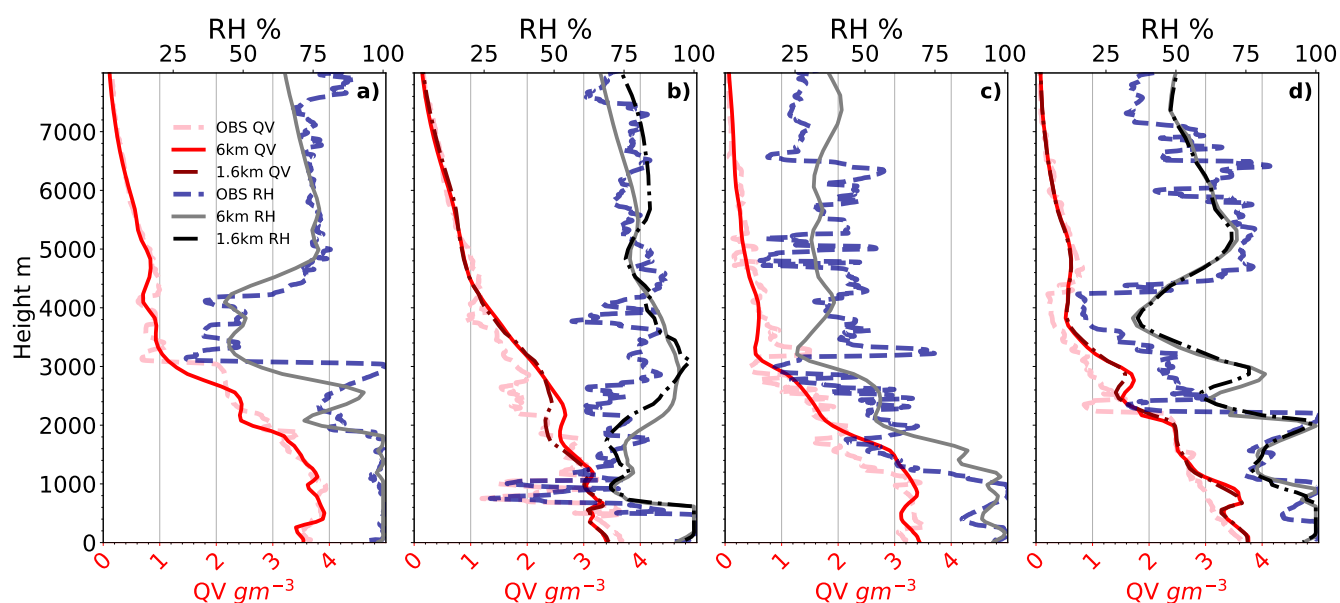
Figure B2. Vertical profiles of moisture content (QV) in red and relative humidity with respect to liquid water (RH) in grey. (a) 1st at initialisation time 00UTC, (b) 1st at 12UTC, (c) 3rd at initialisation time 00UTC, and (d) 3rd at 12UTC. The observational data (in dashed lines) are from the radiosondes (Maturilli et al., 2022) and the model data are the 6 km grid spacing simulation and at 12UTC for both days the 1.6 km simulation is additionally shown (initialisation at 04UTC).
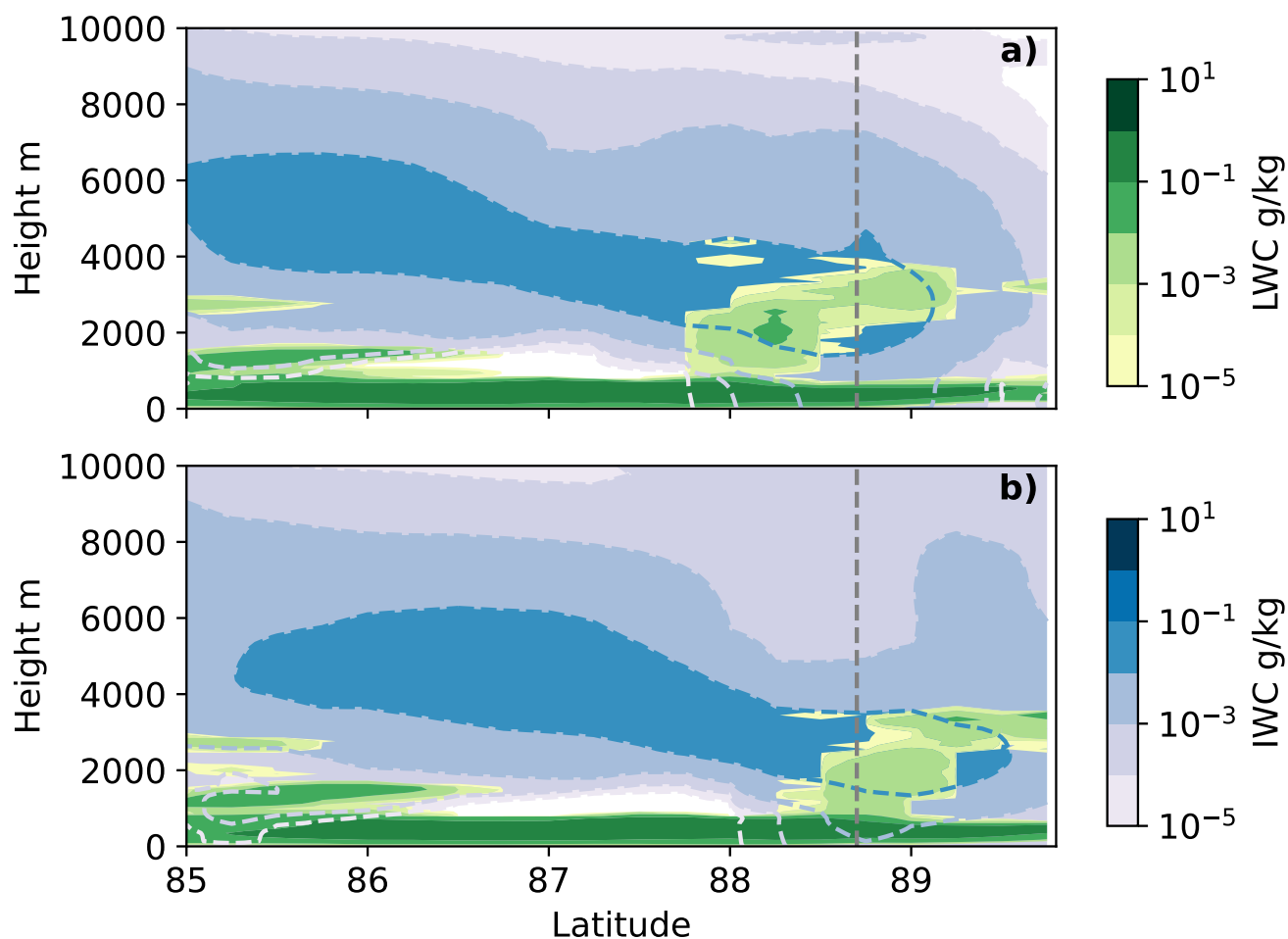
Figure B3. Vertical cross-sections with latitude, from the 1.6 km domain edge at 85°N up to 90°N, the ship location is marked with a dashed vertical line. Shown is the longitudinal mean over the longitudes the back-trajectories span in Fig. B1, indicating the upstream direction of the cloud layers. Shown in green contours is the liquid water content and in blue contours (and dashed outlines) is the ice water content for (a) 10UTC and (b) 12UTC on the 1st of September for the "INP" simulation.
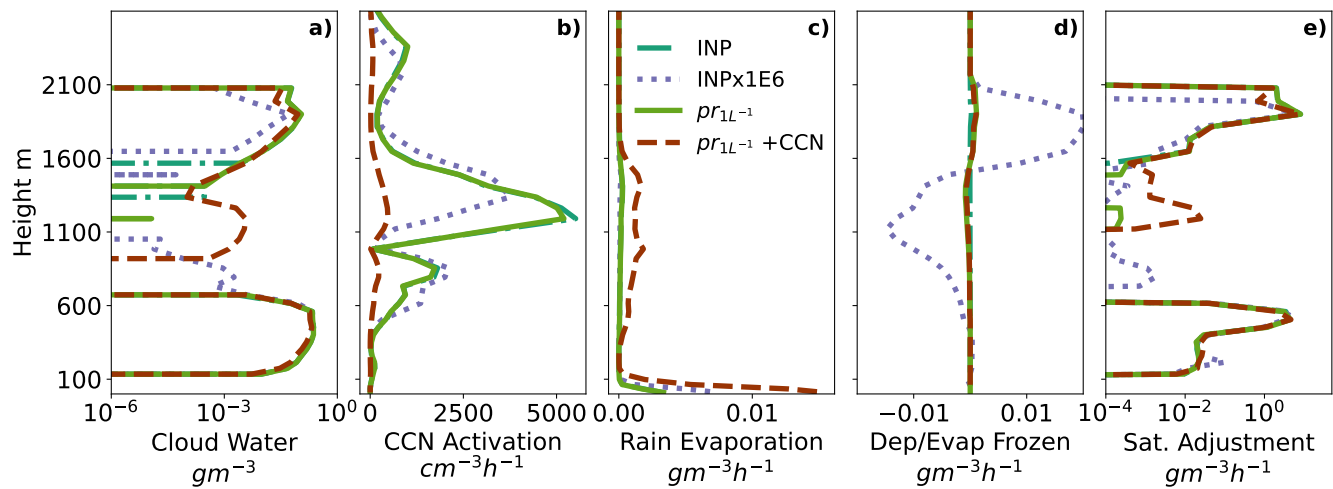
Figure B4. (a) Cloud water mass content for the 3rd of September as a temporal and spatial mean between 06-12UTC, (b) number concentration of cloud droplet activation, (c) evaporation of rain, (d) deposition (positive values) and sublimation (negative values) of ice, snow and graupel, and (e) saturation adjustment, effectively the cloud droplet condensation routine, called to adjust the excess or deficit of vapour.
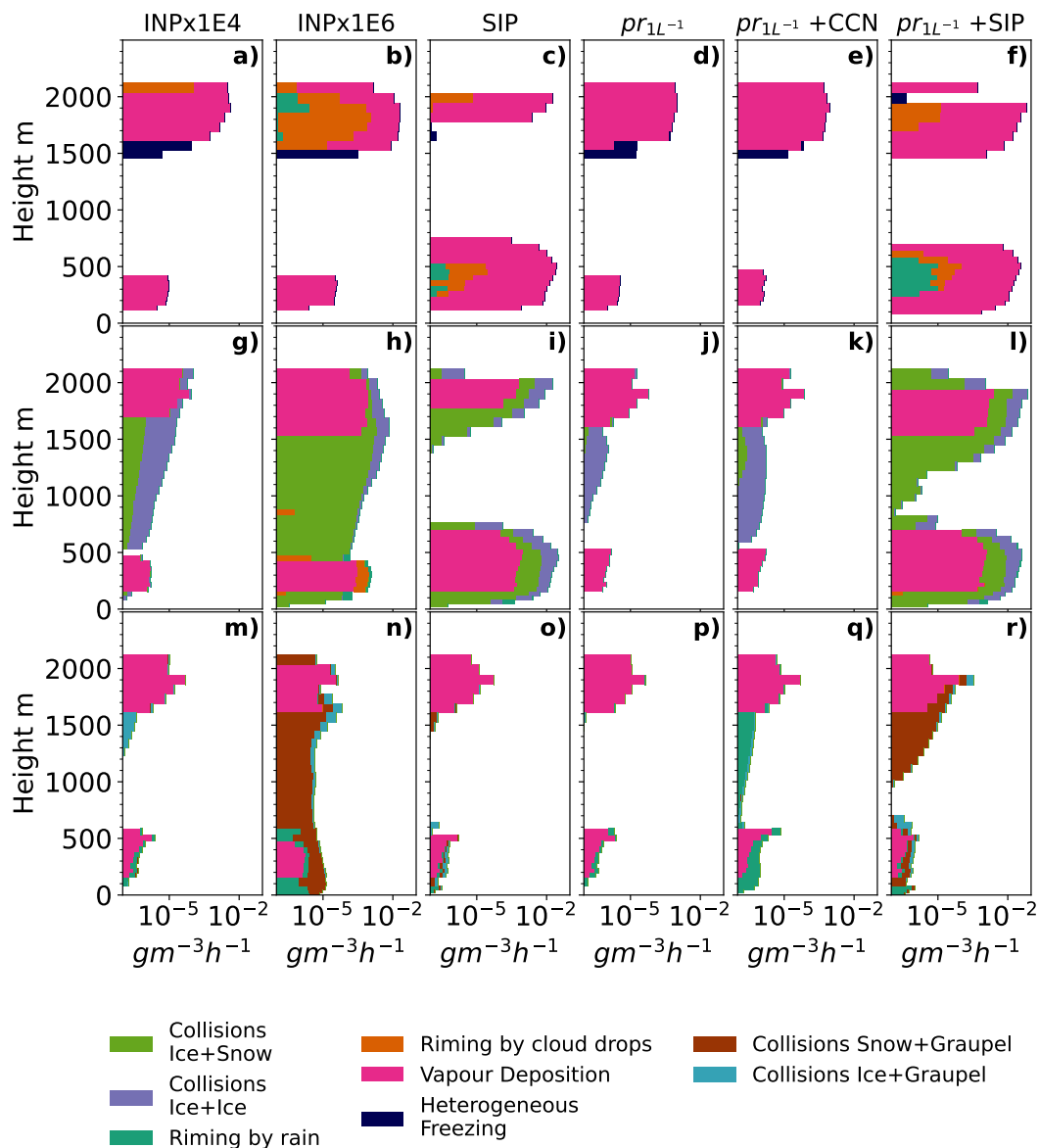
Figure B5. Microphysical process rates accumulated during the simulation and here taken as a mean between 06-12UTC on the 3rd of September. a-f) Show processes contributing to ice mass growth, g-l) for snow and m-r) for graupel. Colours correspond to the various process rates defined in the legend.
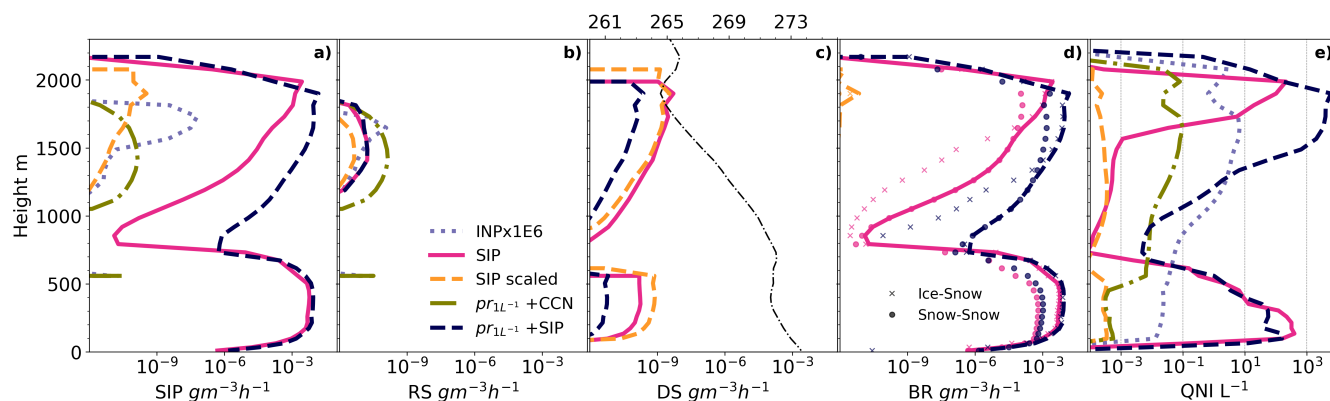
Figure B6. Average secondary ice production rates shown for a select few sensitivity studies on the 3rd of September 2020 between 06UTC-12UTC (before glaciation). (a) All SIP, (b) rime-splintering contribution, (c) droplet freezing and shattering, (d) breakup upon ice-ice collisions with the major contributions snow-ice collisions and snow-snow collisions marked in crosses and circles respectively. Panel e) shows the number concentration of cloud ice where the INP simulation and $pr_{1L^{-1}}$ correspond well to the SIP scaled and $pr_{1L^{-1}}$+ CCN respectively.

Author contributions. GW devised and ran the simulations, wrote the manuscript and led the analysis. AO, LI, PA, MT, and CH provided input and discussions. AO ran the Lagranto trajectories and provided advice and discussions regarding the simulation setup. PA ran the

480 MLC algorithm for the case selection. LI provided in-depth expertise and feedback to the manuscript. CH acquired funding and designed the project.

Competing interests. At least one of the (co-)authors is a member of the editorial board of Atmospheric Chemistry and Physics. The authors have no other competing interests to declare.

Acknowledgements. The authors thank the Bundesministerium für Bildung und Forschung (BMBF) for funding the project with project

485 number 03F0891B. We further thank all those who contributed to MOSAiC and made this endeavour possible (Nixdorf et al., 2021). We acknowledge ACTRIS and the Finnish Meteorological Institute for providing the observational data. This work was carried out on the HoreKa supercomputer funded by the Ministry of Science, Research and the Arts Baden-Württemberg and by the Federal Ministry of Education and Research. The authors would like to thank the Federal Ministry of Education and Research and the state governments (www.nhr-verein.de/unsere-partner) for supporting this project as part of the joint funding of National High-Performance Computing (NHR). This work

490 was performed with the help of the Large Scale Data Facility at the Karlsruhe Institute of Technology funded by the Ministry of Science, Research and the Arts Baden-Württemberg and by the Federal Ministry of Education and Research. Grammarly and ChatGPT have been used for the improvement of the manuscript and plotting scripts. The author would also like to extend special thanks to Jessie Creamean and Matt Shupe for valuable discussions.

References

Abdul-Razzak, H. and Ghan, S. J.: A parameterization of aerosol activation 2. Multiple aerosol types, Journal of Geophysical Research Atmospheres, 105, 6837–6844, https://doi.org/10.1029/1999JD901161, 2000.

Achtert, P., Seelig, T., Wallentin, G., Ickes, L., Hoose, C., and Tesche, M.: Occurrence of multi-layer clouds and ice-crystal seeding in the Arctic: MOSAiC and beyond [In preparation], ACP, 2024.

Ansmann, A., Ohneiser, K., Engelmann, R., Radenz, M., Griesche, H., Hofer, J., Althausen, D., Creamean, J. M., Boyer, M. C., Knopf, D. A., Dahlke, S., Maturilli, M., Gebauer, H., Bühl, J., Jimenez, C., Seifert, P., and Wandinger, U.: Annual cycle of aerosol properties over the central Arctic during MOSAiC 2019–2020 – light-extinction, CCN, and INP levels from the boundary layer to the tropopause, Atmospheric Chemistry and Physics, 23, 12 821–12 849, https://doi.org/10.5194/acp-23-12821-2023, 2023.

Bechtold, P., Köhler, M., Jung, T., Doblas-Reyes, F., Leutbecher, M., Rodwell, M. J., Vitart, F., and Balsamo, G.: Advances in simulating atmospheric variability with the ECMWF model: From synoptic to decadal time-scales, Quarterly Journal of the Royal Meteorological Society, 134, 1337–1351, https://doi.org/https://doi.org/10.1002/qj.289, 2008.

Beck, I., Quéléver, L., Laurila, T., Jokinen, T., Baccarini, A., Angot, H., and Schmale, J.: Pollution mask for the continuous corrected particle number concentration data in 1 min resolution, measured in the Swiss aerosol container during MOSAiC 2019/2020, https://doi.org/10.1594/PANGAEA.941335, 2022.

Bergeron, T.: Über die dreidimensional verknüpfende Wetteranalyse, I kommisjon hos Cammermeyers boghandel, 1928.

Bergner, N., Heutte, B., Angot, H., Dada, L., Beck, I., Quéléver, L., Jokinen, T., Laurila, T., and Schmale, J.: Cloud Condensation Nuclei (CCN) concentrations measured in the Swiss container during MOSAiC 2019/2020, https://doi.org/10.1594/PANGAEA.961131, 2023.

Bigg, E. K.: The formation of atmospheric ice crystals by the freezing of droplets, Quarterly Journal of the Royal Meteorological Society, 79, 510–519, https://doi.org/10.1002/qj.49707934207, 1953.

Bulatovic, I., Savre, J., Tjernström, M., Leck, C., and Ekman, A. M. L.: Large-eddy simulation of a two-layer boundary-layer cloud system from the Arctic Ocean 2018 expedition, Atmospheric Chemistry and Physics, 23, 7033–7055, https://doi.org/10.5194/acp-2022-809, 2023.

Burrows, S. M., McCluskey, C. S., Cornwell, G., Steinke, I., Zhang, K., Zhao, B., Zawadowicz, M., Raman, A., Kulkarni, G., China, S., Zelenyuk, A., and DeMott, P. J.: Ice-Nucleating Particles That Impact Clouds and Climate: Observational and Modeling Research Needs, https://doi.org/10.1029/2021RG000745, 2022.

Chen, Y. S., Harrington, J. Y., Verlinde, J., Zhang, F., and Oue, M.: Dynamical Response of an Arctic Mixed-Phase Cloud to Ice Precipitation and Downwelling Longwave Radiation From an Upper-Level Cloud, Journal of Geophysical Research: Atmospheres, 125, https://doi.org/10.1029/2019JD031089, 2020.

Christensen, M. W., Carrió, G. G., Stephens, G. L., and Cotton, W. R.: Radiative impacts of free-tropospheric clouds on the properties of marine stratocumulus, Journal of the Atmospheric Sciences, 70, 3102–3118, https://doi.org/10.1175/JAS-D-12-0287.1, 2013.

Cooper, W. A.: Ice Initiation in Natural Clouds, Meteorological Monographs, 21, 29 – 32, https://doi.org/10.1175/0065-9401-21.43.29, 1986.

Creamean, J., Hill, T., Demott, P., Barry, K., and Hume, C.: Arctic Ice Nucleation Sampling during MOSAiC (INPMOSAIC2) Field Campaign Report, Tech. rep., 2021a.

Creamean, J. M., De Boer, G., Telg, H., Mei, F., Dexheimer, D., Shupe, M. D., Solomon, A., and McComiskey, A.: Assessing the vertical structure of Arctic aerosols using balloon-borne measurements, Atmospheric Chemistry and Physics, 21, 1737–1757, https://doi.org/10.5194/acp-21-1737-2021, 2021b.

530 Creamean, J. M., Barry, K., Hill, T. C., Hume, C., DeMott, P. J., Shupe, M. D., Dahlke, S., Willmes, S., Schmale, J., Beck, I., Hoppe, C. J., Fong, A., Chamberlain, E., Bowman, J., Scharien, R., and Persson, O.: Annual cycle observations of aerosols capable of ice formation in central Arctic clouds, Nature Communications, 13, https://doi.org/10.1038/s41467-022-31182-x, 2022.

Dada, L., Angot, H., Beck, I., Baccarini, A., Quéléver, L. L., Boyer, M., Laurila, T., Brasseur, Z., Jozef, G., de Boer, G., Shupe, M. D., Henning, S., Bucci, S., Dütsch, M., Stohl, A., Petäjä, T., Daellenbach, K. R., Jokinen, T., and Schmale, J.: A central arctic extreme aerosol
535   event triggered by a warm air-mass intrusion, Nature Communications, 13, https://doi.org/10.1038/s41467-022-32872-2, 2022.

Dedekind, Z., Lauber, A., Ferrachat, S., and Lohmann, U.: Sensitivity of precipitation formation to secondary ice production in winter orographic mixed-phase clouds, Atmospheric Chemistry and Physics, 21, 15 115–15 134, https://doi.org/10.5194/acp-21-15115-2021, 2021.

Dedekind, Z., Proske, U., Ferrachat, S., Lohmann, U., and Neubauer, D.: Simulating the seeder–feeder impacts on cloud ice and precipitation
540   over the Alps, Atmospheric Chemistry and Physics, 24, 5389–5404, https://doi.org/10.5194/acp-24-5389-2024, 2024.

DeMott, P. J., Hill, T. C., McCluskey, C. S., Prather, K. A., Collins, D. B., Sullivan, R. C., Ruppel, M. J., Mason, R. H., Irish, V. E., Lee, T., Hwang, C. Y., Rhee, T. S., Snider, J. R., McMeeking, G. R., Dhaniyala, S., Lewis, E. R., Wentzell, J. J., Abbatt, J., Lee, C., Sultana, C. M., Ault, A. P., Axson, J. L., Martinez, M. D., Venero, I., Santos-Figueroa, G., Stokes, M. D., Deane, G. B., Mayol-Bracero, O. L., Grassian, V. H., Bertram, T. H., Bertram, A. K., Moffett, B. F., and Franc, G. D.: Sea spray aerosol as a unique
545   source of ice nucleating particles, Proceedings of the National Academy of Sciences of the United States of America, 113, 5797–5803, https://doi.org/10.1073/pnas.1514034112, 2016.

Engelmann, R., Althausen, D., Baars, H., Griesche, H., Hofer, J., Radenz, M., and Seifert, P.: Custom collection of categorize, classification, droplet effective radius, ice effective radius, ice water content, and 2 other products from RV Polarstern between 1 and 3 Sep 2020, https://cloudnet.fmi.fi/collection/d342273f-413b-46a0-95ea-985f863f9b79, 2023.

550 Findeisen, W.: Kolloid-meteorologische Vorgänge bei Niederschlagsbildung, Meteorol. Z, 55, 121–133, 1938.

Frisch, A. S.: On cloud radar and microwave radiometer measurements of stratus cloud liquid water profiles, Journal of Geophysical Research Atmospheres, 103, 23 195–23 197, https://doi.org/10.1029/98JD01827, 1998.

Fu, S., Deng, X., Shupe, M. D., and Xue, H.: A modelling study of the continuous ice formation in an autumnal Arctic mixed-phase cloud case, Atmospheric Research, 228, 77–85, https://doi.org/10.1016/j.atmosres.2019.05.021, 2019.

555 Georgakaki, P., Sotiropoulou, G., Vignon, E., Billault-Roux, A. C., Berne, A., and Nenes, A.: Secondary ice production processes in wintertime alpine mixed-phase clouds, Atmospheric Chemistry and Physics, 22, 1965–1988, https://doi.org/10.5194/acp-22-1965-2022, 2022.

Griesche, H. J., Seifert, P., Engelmann, R., Radenz, M., Hofer, J., Althausen, D., Walbröl, A., Barrientos-Velasco, C., Baars, H., Dahlke, S., Tukiainen, S., and Macke, A.: Cloud micro- and macrophysical properties from ground-based remote sensing during the MOSAiC drift experiment, Scientific Data, 11, https://doi.org/10.1038/s41597-024-03325-w, 2024.

560 Hallet, J. and Mossop S.C: Production of secondary ice particles during the riming process, Nature, 249, 26–28, 1974.

Han, C., Hoose, C., and Dürlich, V.: Secondary ice production in simulated deep convective clouds: A sensitivity study, Journal of the Atmospheric Sciences, https://doi.org/10.1175/JAS-D-23-0156.1, 2024.

Hande, L. B., Engler, C., Hoose, C., and Tegen, I.: Seasonal variability of Saharan desert dust and ice nucleating particles over Europe, Atmospheric Chemistry and Physics, 15, 4389–4397, https://doi.org/10.5194/acp-15-4389-2015, 2015.

565 Hande, L. B., Engler, C., Hoose, C., and Tegen, I.: Parameterizing cloud condensation nuclei concentrations during HOPE, Atmospheric Chemistry and Physics, 16, 12 059–12 079, https://doi.org/10.5194/acp-16-12059-2016, 2016.

Harrington, J. Y., Reisin, T., Cotton, W. R., and Kreidenweis, S. M.: Cloud resolving simulations of Arctic stratus Part II: Transition-season clouds, Tech. rep., 1999.

Herman, G. and Goody, R.: Formation and Persistence of Summertime Arctic Stratus Clouds, Journal of Atmospheric Sciences, 33, 1537 –
570   1553, https://doi.org/https://doi.org/10.1175/1520-0469(1976)033<1537:FAPOSA>2.0.CO;2, 1976.

Hogan, R. J. and Bozzo, A.: A Flexible and Efficient Radiation Scheme for the ECMWF Model, Journal of Advances in Modeling Earth Systems, 10, 1990–2008, https://doi.org/10.1029/2018MS001364, 2018.

Hogan, R. J., Mittermaier, M. P., and Illingworth, A. J.: The Retrieval of Ice Water Content from Radar Reflectivity Factor and Temperature and Its Use in Evaluating a Mesoscale Model, Journal of Applied Meteorology and Climatology, 45, 301 – 317,
575   https://doi.org/https://doi.org/10.1175/JAM2340.1, 2006.

Hoose, C. and Möhler, O.: Heterogeneous ice nucleation on atmospheric aerosols: A review of results from laboratory experiments, https://doi.org/10.5194/acp-12-9817-2012, 2012.

Illingworth, A. J., Hogan, R. J., O'Connor, E., Bouniol, D., Brooks, M. E., Delanoé, J., Donovan, D. P., Eastment, J. D., Gaussiat, N., Goddard, J. W. F., Haeffelin, M., Baltink, H. K., Krasnov, O. A., Pelon, J., Piriou, J.-M., Protat, A., Russchenberg, H. W. J., Seifert,
580   A., Tompkins, A. M., van Zadelhoff, G.-J., Vinit, F., Willén, U., Wilson, D. R., and Wrench, C. L.: Cloudnet, Bulletin of the American Meteorological Society, 88, 883–898, https://doi.org/10.1175/BAMS-88-6-883, 2007.

Intrieri, J. M., Shupe, M. D., Uttal, T., and McCarty, B. J.: An annual cycle of Arctic cloud characteristics observed by radar and lidar at SHEBA, Journal of Geophysical Research: Oceans, 107, https://doi.org/10.1029/2000jc000423, 2002.

Jian, B., Li, J., Zhang, L., Wang, Y., Zhang, W., and Li, Y.: Competition Between Radiative and Seeding Effects of Overlying Clouds on
585   Underlying Marine Stratocumulus, Geophysical Research Letters, 49, https://doi.org/10.1029/2022GL100729, 2022.

Kiszler, T., Ebell, K., and Schemann, V.: A Performance Baseline for the Representation of Clouds and Humidity in Cloud-Resolving ICON-LEM Simulations in the Arctic, Journal of Advances in Modeling Earth Systems, 15, https://doi.org/10.1029/2022MS003299, 2023.

Klein, S. A., McCoy, R. B., Morrison, H., Ackerman, A. S., Avramov, A., Boer, G. d., Chen, M., Cole, J. N. S., Del Genio, A. D., Falk, M., Foster, M. J., Fridlind, A., Golaz, J.-C., Hashino, T., Harrington, J. Y., Hoose, C., Khairoutdinov, M. F., Larson, V. E., Liu,
590   X., Luo, Y., McFarquhar, G. M., Menon, S., Neggers, R. A. J., Park, S., Poellot, M. R., Schmidt, J. M., Sednev, I., Shipway, B. J., Shupe, M. D., Spangenberg, D. A., Sud, Y. C., Turner, D. D., Veron, D. E., Salzen, K. v., Walker, G. K., Wang, Z., Wolf, A. B., Xie, S., Xu, K.-M., Yang, F., and Zhang, G.: Intercomparison of model simulations of mixed-phase clouds observed during the ARM Mixed-Phase Arctic Cloud Experiment. I: single-layer cloud, Quarterly Journal of the Royal Meteorological Society, 135, 979–1002, https://doi.org/https://doi.org/10.1002/qj.416, 2009.

595   Kleinheins, J., Kiselev, A., Keinert, A., Kind, M., and Leisner, T.: Thermal Imaging of Freezing Drizzle Droplets: Pressure Release Events as a Source of Secondary Ice Particles, American Meteorological Society, 78, 1703–1713, https://doi.org/10.1175/JAS-D-20, 2021.

Knust, R.: Polar Research and Supply Vessel POLARSTERN Operated by the Alfred-Wegener-Institute, Journal of large-scale research facilities JLSRF, 3, A119, https://doi.org/10.17815/jlsrf-3-163, 2017.

Komurcu, M., Storelvmo, T., Tan, I., Lohmann, U., Yun, Y., Penner, J. E., Wang, Y., Liu, X., and Takemura, T.: Intercomparison of the cloud
600   water phase among global climate models, Journal of Geophysical Research, 119, 3372–3400, https://doi.org/10.1002/2013JD021119, 2014.

Koontz, A., Uin, J., Andrews, E., Enekwizu, O., Hayes, C., and Salwen, C.: Cloud Condensation Nuclei Particle Counter (AOSCCN2COLA), https://doi.org/10.5439/1323892, accessed November 8, 2023., 2019.

Korolev, A.: Limitations of the Wegener-Bergeron-Findeisen mechanism in the evolution of mixed-phase clouds, Journal of the Atmospheric
605   Sciences, 64, 3372–3375, https://doi.org/10.1175/JAS4035.1, 2007.

Korolev, A. and Leisner, T.: Review of experimental studies of secondary ice production, Atmospheric Chemistry and Physics, 20, 11 767–
11 797, https://doi.org/10.5194/acp-20-11767-2020, 2020.

Korolev, A., McFarquhar, G., Field, P. R., Franklin, C., Lawson, P., Wang, Z., Williams, E., Abel, S. J., Axisa, D., Borrmann, S., Crosier, J.,
Fugal, J., Krämer, M., Lohmann, U., Schlenczek, O., Schnaiter, M., and Wendisch, M.: Mixed-Phase Clouds: Progress and Challenges,
610   Meteorological Monographs, 58, 1–5, https://doi.org/10.1175/amsmonographs-d-17-0001.1, 2017.

Kretzschmar, J., Stapf, J., Klocke, D., Wendisch, M., and Quaas, J.: Employing airborne radiation and cloud microphysics observations to
improve cloud representation in ICON at kilometer-scale resolution in the Arctic, Atmospheric Chemistry and Physics, 20, 13 145–13 165,
https://doi.org/10.5194/acp-20-13145-2020, 2020.

L'Ecuyer, T. S., Hang, Y., Matus, A. V., and Wang, Z.: American Meteorological Society Reassessing the Effect of Cloud Type
615   on Earth's Energy Balance in the Age of Active Spaceborne Observations. Part I, Source: Journal of Climate, 32, 6197–6217,
https://doi.org/10.2307/26831705, 2019.

Lilly, D. K.: On the numerical simulation of buoyant convection, Tellus, 14, 148–172, https://doi.org/10.1111/j.2153-3490.1962.tb00128.x,
1962.

Liu, Y., Key, J. R., Ackerman, S. A., Mace, G. G., and Zhang, Q.: Arctic cloud macrophysical characteristics from CloudSat and CALIPSO,
620   Remote Sensing of Environment, 124, 159–173, https://doi.org/10.1016/j.rse.2012.05.006, 2012.

Lonardi, M., Pilz, C., Akansu, E. F., Dahlke, S., Egerer, U., Ehrlich, A., Griesche, H., Heymsfield, A. J., Kirbus, B., Schmitt, C. G.,
Shupe, M. D., Siebert, H., Wehner, B., and Wendisch, M.: Tethered balloon-borne profile measurements of atmospheric proper-
ties in the cloudy atmospheric boundary layer over the Arctic sea ice during MOSAiC: Overview and first results, Elementa, 10,
https://doi.org/10.1525/elementa.2021.000120, 2022.

625 López-García, V., Neely, R. R., Dahlke, S., and Brooks, I. M.: Low-level jets over the Arctic Ocean during MOSAiC, Elementa, 10, 4993–
5007, https://doi.org/10.1525/elementa.2022.00063, 2022.

Luo, Y., Xu, K. M., Morrison, H., McFarquhar, G. M., Wang, Z., and Zhang, G.: Multi-layer arctic mixed-phase clouds simulated by a
cloud-resolving model: Comparison with ARM observations and sensitivity experiments, Journal of Geophysical Research Atmospheres,
113, https://doi.org/10.1029/2007JD009563, 2008.

630 Mason, B. J. and Maybank, J.: The fragmentation and electrification of freezing water drops, Quarterly Journal of the Royal Meteorological
Society, 86, 176–185, https://doi.org/10.1002/qj.49708636806, 1960.

Maturilli, M., Sommer, M., Holdridge, D. J., Dahlke, S., and Schulz, A.: Radiosonde measurements in 2020-09 during MOSAiC Legs
PS122/5 (level 3 data), PANGAEA, https://doi.org/10.1594/PANGAEA.944834, in: Maturilli, Marion; Sommer, Michael; Holdridge,
Donna J; Dahlke, Sandro; Graeser, Jürgen; Sommerfeld, Anja; Jaiser, Ralf; Deckelmann, Holger; Schulz, Alexander (2022): MOSAiC
635   radiosonde data (level 3). PANGAEA, https://doi.org/10.1594/PANGAEA.943870, 2022.

Mauritsen, T., Sedlar, J., Tjernström, M., Leck, C., Martin, M., Shupe, M., Sjogren, S., Sierau, B., Persson, P. O., Brooks, I. M., and Swi-
etlicki, E.: An Arctic CCN-limited cloud-aerosol regime, Atmospheric Chemistry and Physics, 11, 165–173, https://doi.org/10.5194/acp-
11-165-2011, 2011.

Morrison, H., Curry, J. A., and Khvorostyanov, V. I.: A New Double-Moment Microphysics Parameterization for Application in Cloud and
640   Climate Models. Part I: Description, Tech. rep., 2005.

Morrison, H., McCoy, R. B., Klein, S. A., Xie, S., Luo, Y., Avramov, A., Chen, M., Cole, J. N., Falk, M., Foster, M. J., del Genio, A. D., Harrington, J. Y., Hoose, C., Khairoutdinov, M. F., Larson, V. E., Liu, X., McFarquhar, G. M., Poellot, M. R., von Salzen, K., Shipway, B. J., Shupe, M. D., Sud, Y. C., Turner, D. D., Veron, D. E., Walker, G. K., Wang, Z., Wolf, A. B., Xu, K. M., Yang, F., and Zhang, G.: Intercomparison of model simulations of mixed-phase clouds observed during the ARM Mixed-Phase Arctic Cloud Experiment. II:
645   Multilayer cloud, Quarterly Journal of the Royal Meteorological Society, 135, 1003–1019, https://doi.org/10.1002/qj.415, 2009.

Morrison, H., De Boer, G., Feingold, G., Harrington, J., Shupe, M. D., and Sulia, K.: Resilience of persistent Arctic mixed-phase clouds, https://doi.org/10.1038/ngeo1332, 2012.

Mossop, S. C.: The Freezing of Supercooled Water, Proceedings of the Physical Society. Section B, 68, 193–208, https://doi.org/10.1088/0370-1301/68/4/301, 1954.

650   Nixdorf, U., Dethloff, K., Rex, M., Shupe, M., Sommerfeld, A., Perovich, D., Nicolaus, M., Heuzé, C., Rabe, B., Loose, B., Damm, E., Gradinger, R., Fong, A., Maslowski, W., Rinke, A., Kwok, R., Spreen, G., Wendisch, M., Herber, A., Hirsekorn, M., Mohaupt, V., Frickenhaus, S., Immerz, A., Weiss-Tuider, K., König, B., Mengedoht, D., Regnery, J., Gerchow, P., Ransby, D., Krumpen, T., Morgenstern, A., Haas, C., Kanzow, T., Rack, F. R., Saitzev, V., Sokolov, V., Makarov, A., Schwarze, S., Wunderlich, T., Wurr, K., and Boetius, A.: MOSAiC Extended Acknowledgement, Tech. rep., 2021.

655   Nomokonova, T., Ebell, K., Löhnert, U., Maturilli, M., Ritter, C., and O'Connor, E.: Statistics on clouds and their relation to thermodynamic conditions at Ny-Ålesund using ground-based sensor synergy, Atmospheric Chemistry and Physics, 19, 4105–4126, https://doi.org/10.5194/acp-19-4105-2019, 2019.

Omanovic, N., Ferrachat, S., Fuchs, C., Henneberger, J., Miller, A. J., Ohneiser, K., Ramelli, F., Seifert, P., Spirig, R., Zhang, H., and Lohmann, U.: Evaluating the Wegener–Bergeron–Findeisen process in ICON in large-eddy mode with in situ observations from the
660   CLOUDLAB project, Atmospheric Chemistry and Physics, 24, 6825–6844, https://doi.org/10.5194/acp-24-6825-2024, 2024.

Ovchinnikov, M., Ackerman, A. S., Avramov, A., Cheng, A., Fan, J., Fridlind, A. M., Ghan, S., Harrington, J., Hoose, C., Korolev, A., McFarquhar, G. M., Morrison, H., Paukert, M., Savre, J., Shipway, B. J., Shupe, M. D., Solomon, A., and Sulia, K.: Intercomparison of large-eddy simulations of Arctic mixed-phase clouds: Importance of ice size distribution assumptions, Journal of Advances in Modeling Earth Systems, 6, 223–248, https://doi.org/10.1002/2013MS000282, 2014.

665   Pasquier, J. T., Henneberger, J., Ramelli, F., Lauber, A., David, R. O., Wieder, J., Carlsen, T., Gierens, R., Maturilli, M., and Lohmann, U.: Conditions favorable for secondary ice production in Arctic mixed-phase clouds, Atmospheric Chemistry and Physics, 22, 15 579–15 601, https://doi.org/10.5194/acp-22-15579-2022, 2022.

Porter, G. C., Adams, M. P., Brooks, I. M., Ickes, L., Karlsson, L., Leck, C., Salter, M. E., Schmale, J., Siegel, K., Sikora, S. N., Tarn, M. D., Vüllers, J., Wernli, H., Zieger, P., Zinke, J., and Murray, B. J.: Highly Active Ice-Nucleating Particles at the Summer North Pole, Journal
670   of Geophysical Research: Atmospheres, 127, https://doi.org/10.1029/2021JD036059, 2022.

Possner, A., Pfannkuch, K., Ramadoss, and V: Cloud-Resolving ICON Simulations of Secondary Ice Production in Arctic Mixed-Phase Stratocumuli Observed during M-PACE, American Meteorological Society, 81, 417–434, https://doi.org/10.1175/JAS-D-23, 2024.

Proske, U., Bessenbacher, V., Dedekind, Z., Lohmann, U., and Neubauer, D.: How frequent is natural cloud seeding from ice cloud layers (&-35&°C) over Switzerland?, Atmospheric Chemistry and Physics, 21, 5195–5216, https://doi.org/10.5194/acp-21-5195-2021, 2021.

675   Purser, R. J.: Accurate Numerical Differencing near a Polar Singularity of a Skipped Grid, Monthly Weather Review, 116, 1067 – 1076, https://doi.org/https://doi.org/10.1175/1520-0493(1988)116<1067:ANDNAP>2.0.CO;2, 1988.

Raif, E. N., Barr, S. L., Tarn, M. D., Mcquaid, J. B., Daily, M. I., Abel, S. J., Barrett, P. A., Bower, K. N., Field, P. R., Carslaw, K. S., and Murray, B. J.: High ice-nucleating particle concentrations associated with Arctic haze in springtime cold-air outbreaks, EGUsphere [preprint], https://doi.org/10.5194/egusphere-2024-1502, 2024.

680 Raschendorfer, M.: The new turbulence parameterization of LM, COSMONewsLetterNo.1,ConsortiumforSmall-ScaleModelling,http://www.cosmo-model.org., 2001.

Schäfer, B., David, R. O., Georgakaki, P., Pasquier, J. T., Sotiropoulou, G., and Storelvmo, T.: Simulations of primary and secondary ice production during an Arctic mixed-phase cloud case from the Ny-Ålesund Aerosol Cloud Experiment (NASCENT) campaign, Atmospheric Chemistry and Physics, 24, 7179–7202, https://doi.org/10.5194/acp-24-7179-2024, 2024.

685 Schmale, J., Zieger, P., and Ekman, A. M.: Aerosols in current and future Arctic climate, Nature Climate Change, 11, 95–105, https://doi.org/10.1038/s41558-020-00969-5, 2021.

Seifert, A. and Beheng, K. D.: A two-moment cloud microphysics parameterization for mixed-phase clouds. Part 1: Model description, Meteorology and Atmospheric Physics, 92, 45–66, https://doi.org/10.1007/s00703-005-0112-4, 2006.

Shupe, M. D.: Clouds at arctic atmospheric observatories. Part II: Thermodynamic phase characteristics, Journal of Applied Meteorology
690 and Climatology, 50, 645–661, https://doi.org/10.1175/2010JAMC2468.1, 2011.

Shupe, M. D. and Matrosov, S. Y.: Arctic Mixed-Phase Cloud Properties Derived from Surface-Based Sensors at SHEBA, Tech. rep., 2006.

Shupe, M. D., Uttal, T., and Matrosov, S. Y.: Arctic Cloud Microphysics Retrievals from Surface-Based Remote Sensors at SHEBA, Journal of Applied Meteorology, 44, 1544 – 1562, https://doi.org/https://doi.org/10.1175/JAM2297.1, 2005.

Shupe, M. D., Persson, P. O., Brooks, I. M., Tjernström, M., Sedlar, J., Mauritsen, T., Sjogren, S., and Leck, C.: Cloud and boundary layer
695 interactions over the Arctic sea ice in late summer, Atmospheric Chemistry and Physics, 13, 9379–9400, https://doi.org/10.5194/acp-13-9379-2013, 2013.

Shupe, M. D., Rex, M., Blomquist, B., G. Persson, P. O., Schmale, J., Uttal, T., Althausen, D., Angot, H., Archer, S., Bariteau, L., Beck, I., Bilberry, J., Bucci, S., Buck, C., Boyer, M., Brasseur, Z., Brooks, I. M., Calmer, R., Cassano, J., Castro, V., Chu, D., Costa, D., Cox, C. J., Creamean, J., Crewell, S., Dahlke, S., Damm, E., de Boer, G., Deckelmann, H., Dethloff, K., Dütsch, M., Ebell, K., Ehrlich, A., Ellis,
700 J., Engelmann, R., Fong, A. A., Frey, M. M., Gallagher, M. R., Ganzeveld, L., Gradinger, R., Graeser, J., Greenamyer, V., Griesche, H., Griffiths, S., Hamilton, J., Heinemann, G., Helmig, D., Herber, A., Heuzé, C., Hofer, J., Houchens, T., Howard, D., Inoue, J., Jacobi, H. W., Jaiser, R., Jokinen, T., Jourdan, O., Jozef, G., King, W., Kirchgaessner, A., Klingebiel, M., Krassovski, M., Krumpen, T., Lampert, A., Landing, W., Laurila, T., Lawrence, D., Lonardi, M., Loose, B., Lüpkes, C., Maahn, M., Macke, A., Maslowski, W., Marsay, C., Maturilli, M., Mech, M., Morris, S., Moser, M., Nicolaus, M., Ortega, P., Osborn, J., Pätzold, F., Perovich, D. K., Petäjä, T., Pilz, C., Pirazzini,
705 R., Posman, K., Powers, H., Pratt, K. A., Preußer, A., Quéléver, L., Radenz, M., Rabe, B., Rinke, A., Sachs, T., Schulz, A., Siebert, H., Silva, T., Solomon, A., Sommerfeld, A., Spreen, G., Stephens, M., Stohl, A., Svensson, G., Uin, J., Viegas, J., Voigt, C., von der Gathen, P., Wehner, B., Welker, J. M., Wendisch, M., Werner, M., Xie, Z. Q., and Yue, F.: Overview of the MOSAiC expedition- Atmosphere, https://doi.org/10.1525/elementa.2021.00060, 2022.

Silber, I. and Shupe, M. D.: Insights on sources and formation mechanisms of liquid-bearing clouds over MOSAiC examined from a La-
710 grangian framework, Elementa, 10, https://doi.org/10.1525/elementa.2021.000071, 2022.

Smagorinsky, J.: General circulation experiments with the primitive equations: I. The basic experiment, Monthly weather review, 91, 99–164, 1963.

Solomon, A., Feingold, G., and Shupe, M. D.: The role of ice nuclei recycling in the maintenance of cloud ice in Arctic mixed-phase stratocumulus, Atmospheric Chemistry and Physics, 15, 10 631–10 643, https://doi.org/10.5194/acp-15-10631-2015, 2015.

715 Solomon, A., De Boer, G., Creamean, J. M., McComiskey, A., Shupe, M. D., Maahn, M., and Cox, C.: The relative impact of cloud conden-
sation nuclei and ice nucleating particle concentrations on phase partitioning in Arctic mixed-phase stratocumulus clouds, Atmospheric
Chemistry and Physics, 18, 17 047–17 059, https://doi.org/10.5194/acp-18-17047-2018, 2018.

Sotiropoulou, G., Sullivan, S., Savre, J., Lloyd, G., Lachlan-Cope, T., Ekman, A. M., and Nenes, A.: The impact of secondary ice production
on Arctic stratocumulus, Atmospheric Chemistry and Physics, 20, 1301–1316, https://doi.org/10.5194/acp-20-1301-2020, 2020.

720 Sotiropoulou, G., Vignon, E., Young, G., Morrison, H., O'Shea, S. J., Lachlan-Cope, T., Berne, A., and Nenes, A.: Secondary ice production
in summer clouds over the Antarctic coast: An underappreciated process in atmospheric models, Atmospheric Chemistry and Physics, 21,
755–771, https://doi.org/10.5194/acp-21-755-2021, 2021.

Sotiropoulou, G., Lewinschal, A., Georgakaki, P., Phillips, V. T. J., Patade, S., Ekman, A. M. L., and Nenes, A.: Sensitivity of Arctic Clouds
to Ice Microphysical Processes in the NorESM2 Climate Model, American Meteorological Society, 37, https://doi.org/10.1175/JCLI-D-
725 22-0458.s1, 2024.

Sprenger, M. and Wernli, H.: The LAGRANTO Lagrangian analysis tool - Version 2.0, Geoscientific Model Development, 8, 2569–2586,
https://doi.org/10.5194/gmd-8-2569-2015, 2015.

Sterzinger, L. J., Sedlar, J., Guy, H., Neely, R. R., and Igel, A. L.: Do Arctic mixed-phase clouds sometimes dissipate due to insufficient
aerosol? Evidence from comparisons between observations and idealized simulations, Atmospheric Chemistry and Physics, 22, 8973–
730 8988, https://doi.org/10.5194/acp-22-8973-2022, 2022.

Subrahmanyam, K. V. and Kumar, K. K.: CloudSat observations of multi layered clouds across the globe, Climate Dynamics, 49, 327–341,
https://doi.org/10.1007/s00382-016-3345-7, 2017.

Sullivan, S. C., Barthlott, C., Crosier, J., Zhukov, I., Nenes, A., and Hoose, C.: The effect of secondary ice production parameterization on
the simulation of a cold frontal rainband, Atmospheric Chemistry and Physics, 18, 16 461–16 480, https://doi.org/10.5194/acp-18-16461-
735 2018, 2018.

Takahashi, T., Nagao, Y., and Kushiyama, Y.: Possible High Ice Particle Production during Graupel-Graupel Collisions, American Meteoro-
logical Society, 52, 4523–4527, 1995.

Tan, I. and Storelvmo, T.: Evidence of Strong Contributions From Mixed-Phase Clouds to Arctic Climate Change, Geophysical Research
Letters, 46, 2894–2902, https://doi.org/10.1029/2018GL081871, 2019.

740 Tiedtke, M.: A Comprehensive Mass Flux Scheme for Cumulus Parameterization in Large-Scale Models, Monthly Weather Review, 117,
1779 – 1800, https://doi.org/https://doi.org/10.1175/1520-0493(1989)117<1779:ACMFSF>2.0.CO;2, 1989.

Tjernström, M. and Graversen, R. G.: The vertical structure of the lower Arctic troposphere analysed from observati0ns and the ERA-40
reanalysis, Quarterly Journal of the Royal Meteorological Society, 135, 431–443, https://doi.org/10.1002/qj.380, 2009.

Turner, D. D., Shupe, M. D., and Zwink, A. B.: Characteristic atmospheric radiative heating rate profiles in arctic clouds as observed at
745 Barrow, Alaska, Journal of Applied Meteorology and Climatology, 57, 953–968, https://doi.org/10.1175/JAMC-D-17-0252.1, 2018.

Udisti, R., Bazzano, A., Becagli, S., Bolzacchini, E., Caiazzo, L., Cappelletti, D., Ferrero, L., Frosini, D., Giardi, F., Grotti, M., Lupi,
A., Malandrino, M., Mazzola, M., Moroni, B., Severi, M., Traversi, R., Viola, A., and Vitale, V.: Sulfate source apportionment in the
Ny-Ålesund (Svalbard Islands) Arctic aerosol, Rendiconti Lincei, 27, 85–94, https://doi.org/10.1007/s12210-016-0517-7, 2016.

Vassel, M., Ickes, L., Maturilli, M., and Hoose, C.: Classification of Arctic multilayer clouds using radiosonde and radar data in Svalbard,
750 Atmospheric Chemistry and Physics, 19, 5111–5126, https://doi.org/10.5194/acp-19-5111-2019, 2019.

Vüllers, J., Achtert, P., Brooks, I. M., Tjernström, M., Prytherch, J., Burzik, A., and Neely III, R.: Meteorological and cloud conditions during
the Arctic Ocean 2018 expedition, Atmospheric Chemistry and Physics, 21, 289–314, https://doi.org/10.5194/acp-21-289-2021, 2021.

Wang, T., Fetzer, E. J., Wong, S., Kahn, B. H., and Yue, Q.: Validation of MODIS cloud mask and multilayer flag using CloudSat-CALIPSO cloud profiles and a cross-reference of their cloud classifications, Journal of Geophysical Research: Atmospheres, 121, https://doi.org/10.1002/2016JD025239, 2016.

Wegener, A.: Thermodynamik der atmosphäre, Leipzig, Germany; Barth, 1911.

Wernli, H. and Davies, H. C.: A Lagrangian-based analysis of extratropical cyclones. I: The method and some applications, Quarterly Journal of the Royal Meteorological Society, 123, 467–489, https://doi.org/https://doi.org/10.1002/qj.49712353811, 1997.

Zängl, G., Reinert, D., Rípodas, P., and Baldauf, M.: The ICON (ICOsahedral Non-hydrostatic) modelling framework of DWD and MPI-M: Description of the non-hydrostatic dynamical core, Quarterly Journal of the Royal Meteorological Society, 141, 563–579, https://doi.org/10.1002/qj.2378, 2015.

Zhao, X. and Liu, X.: Primary and secondary ice production: Interactions and their relative importance, Atmospheric Chemistry and Physics, 22, https://doi.org/10.5194/acp-22-2585-2022, 2022.

Zhao, X., Liu, X., Phillips, V. T., and Patade, S.: Impacts of secondary ice production on Arctic mixed-phase clouds based on ARM observations and CAM6 single-column model simulations, Atmospheric Chemistry and Physics, 21, 5685–5703, https://doi.org/10.5194/acp-21-5685-2021, 2021.

Zieger, P., Heslin-Rees, D., Karlsson, L., Koike, M., Modini, R., and Krejci, R.: Black carbon scavenging by low-level Arctic clouds, Nature Communications, 14, https://doi.org/10.1038/s41467-023-41221-w, 2023.